DETERMINATION OF LONGITUDINAL STRESS IN RAILS

A Thesis

by

FERDINAND DJAYAPUTRA

Submitted to the Office of Graduate Studies of
Texas A&M University
in partial fulfillment of the requirements for the degree of

MASTER OF SCIENCE

December 2010

Major Subject: Civil Engineering

DETERMINATION OF LONGITUDINAL STRESS IN RAILS

A Thesis

by

FERDINAND DJAYAPUTRA

Submitted to the Office of Graduate Studies of
Texas A&M University
in partial fulfillment of the requirements for the degree of

MASTER OF SCIENCE

Approved by:

Chair of Committee,   Stefan Hurlebaus
Committee Members,   Gary Fry
    Don Bray
Head of Department,   John Niedzwecki

December 2010

Major Subject: Civil Engineering

ABSTRACT

Determination of Longitudinal Stress in Rails. (December 2010)

Ferdinand Djayaputra, B.S., Texas A&M University

Chair of Advisory Committee: Dr. Stefan Hurlebaus

The objective of this research is to determine the longitudinal stress in rails by using the polarization of Rayleigh waves. Analytical models are developed to describe the effect of applied stress on wave speed and on the polarization of Rayleigh waves. A numerical simulation is performed to find the effect of applied stress on wave velocity and Rayleigh wave polarization. The effect of uncertainties in material properties on wave velocity and polarization of Rayleigh wave is also examined in the simulation. The experiment uses a laser Doppler vibrometer (LDV) to measure the particle velocities. The in-plane and out-of-plane velocity components are obtained from the measured particle velocities. The polarization of Rayleigh wave, which is defined as the ratio between the in-plane and out-of-plane displacements, is calculated. Furthermore, the polarization of the Rayleigh wave is considered as a measure to identify applied stress. The experiment is performed on unstressed and stressed rail specimen. Thus, Rayleigh wave polarization is obtained as a function of applied stress. The experimental results are compared with the analytical model. The result shows a good agreement with the theoretical values for unstressed rail.

ACKNOWLEDGEMENTS

TABLE OF CONTENTS

LIST OF FIGURES

Page

LIST OF TABLES

CHAPTER I

INTRODUCTION

1.1. Background

Continuous welded rails (CWR) are rails that are welded together to become long continuous members. Using CWR will ensure a smooth ride and reduce unneeded abrasion. The main issue with using CWR is the temperature induced stress. Unconstrained rail steel expands in hot weather and shrinks in cold weather. Due to fixed ends, the rails are restrained from expanding and shrinking. Hence, the rails will experience a compressive stress in hot weather and they will undergo a tensile stress in cold conditions.

Fig. 1.1 – Rail buckling (Telegraph Media Group, 2010)

_____

This thesis follows the style of the *ASCE Journal of Structural Engineering*.

The temperature at which the rails experience zero stress is called the rail neutral temperature (RNT). A large difference between the RNT and the surrounding temperature can cause the rails to buckle or fracture. Fig. 1.1 shows how the rails could buckle due to a large difference between RNT and ambient temperature.

To prevent this problem, the rails are installed at the temperature between hot and cold conditions; thus, setting up the RNT to be in between the buckling and fracturing region. Kish and Samavedam (2005) identified that RNT of rail steel could change due to several factors such as rail movement through fasteners. Moreover, the temperature of the rail can exceed the ambient temperature by around 15°C in hot weather, causing the rail steel to reach temperatures of 45°C when the ambient temperature is 30°C. This result causes a greater chance of rail buckling. For example, a CWR is installed at 25°C (RNT = 25°C). Consider that rail buckling happens at a temperature difference of 20°C. Thus, the rail will buckle when the temperature reaches to 45°C. Due to the rail movement through the fastener, the RNT drops to 15°C. This change in RNT causes the rail to buckle when the temperature reaches 35°C.

The example above shows how important it is to keep inspecting the rail neutral temperature of CWR. Installing CWR at a "safe" region between buckling and fracturing temperatures does not guarantee that the rail will not buckle in the future. Hence, in order to prevent the rails from buckling or fracturing, RNT needs to be identified on a timely basis.

1.2 Research Objective

The objective of this research is to identify the longitudinal stress in a rail by using the polarization of Rayleigh waves to ensure that rail is installed at the proper temperature. This research utilizes the acoustoelastic effect of Rayleigh waves to determine the stress in the rail.

In the experimental procedure, the ultrasonic waves are generated by a transducer, and a laser Doppler vibrometer (Hurlebaus and Jacobs, 2006) is used to measure both the in-plane and out-of-plane velocity components of the Rayleigh wave. The results are processed to obtain the Rayleigh wave polarization which is used to identify the longitudinal stress. Once the longitudinal stress is identified, and the ambient temperature is measured, the RNT is be calculated by

$$T_n = T_a - \frac{\sigma}{E\alpha} \quad , \tag{1.1}$$

where T_n is the rail neutral temperature, T_a is the ambient temperature, σ is the residual stress, E is Young's Modulus, and α is the thermal expansion coefficient. The graph of this relationship can be seen in Fig. 1.2. Once the RNT is determined, the conditions of the rails can be evaluated, and decisions can be if maintainance is necessary to increase safety.
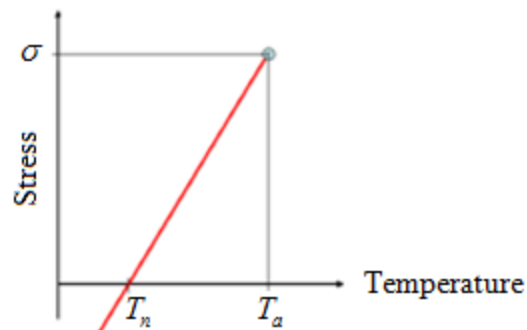
Fig. 1.2 – Rail neutral temperature

1.3 Organization of Thesis

This thesis is divided into eight chapters. Chapter I introduces the background of this research and the objective of this investigation. Chapter II gives details on the literature review on the background of acoustoelasticity and the methods of measuring longitudinal stress in rails. The theoretical background of Rayleigh waves is discussed in Chapter III. Chapter IV describes the analytical model that explains the polarization of Rayleigh waves. In Chapter V, the numerical solution to the propagation of Rayleigh waves is explained. Chapter VI presents the experimental setup and procedure used in the experiment. The results of this experiment are explained in Chapter VII. The summary of the work, along with the conclusions and the recommendations for future work of this research, can be found in Chapter VIII.

CHAPTER II

LITERATURE REVIEW

This chapter presents the various methods of measuring longitudinal stress in rails along with some of the limitations. The chapter also explains the acoustoelastic effect and some previous research that utilized the acoustoelasticity as part of their investigations.

2.1 Methods of Stress Measurements

There are many methods of stress measurements that have been used by the rail road industries. Using traditional technique, stress can be measured by cutting the rail, measuring the gap, calculating the RNT, and re-welding the rail. This method is a destructive measurement, labor intensive, and costly. The VERSE method (Tunna, 2000), shown in Fig. 2.1, measures the stress non-destructively. In this method, the rail is unclipped and lifted, a set of loads is then applied, the displacement is monitored, and the rail is re-clipped. Although this method is non-destructive, this technique is labor and measurement intensive; thus, it is time consuming and costly.

Fig. 2.1 – VERSE equipment (Net Resources International, 2010)

The d'Stresen technique (Kish and Read, 2006) identifies that the vibration amplitude of a rail is proportional to the longitudinal force in the rail. The amplitude of vibration is at maximum when the rail has no stress. Therefore, the RNT can be determined. The results from using d'Stresen system were compared to the RNT values calculated from using strain gauges technique. The results showed good agreement between the two techniques. However, the d'Stresen system works only when the rail is under tension. Also, this technique is a contact measurement method; thus, it cannot be applied on a running train.

Damljanovic and Weaver (2005) investigated the non-destructive measurement of longitudinal stress in rails by measuring the lateral bending wavenumber when the rail was stressed, and compared it with the lateral bending wavenumber of the unstressed rail at a fixed frequency. The principle of this technique is that the stress affects the wavelength of bending waves. In practice, this technique requires very high precision equipment to measure the lateral bending wavenumber.

A recent development on determining RNT or stress free temperature (SFT) in rails is the magnetic system (MAPS Technology, 2007). This system is based on the sensitivity of magnetic properties to stress. Ferromagnetic materials, such as rail steel, have a magnetic structure that is divided into domains that are aligned along the direction of their magnetization. MAPS-SFT analyzes the change in the magnetic properties of the rail that is triggered by the change in the domain alignment due to the presence of stress. The configuration of MAPS-SFT can be seen in Fig 2.2.
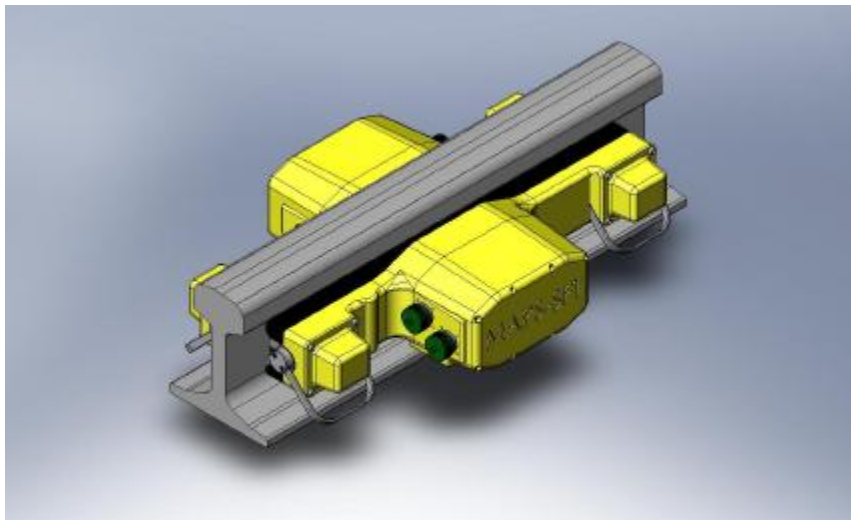
Fig. 2.2 – MAPS-SFT system (*Hayes, 2008*)

MAPS technology measures the total stress of both applied stress and residual stress (Hayes, 2008). MAPS-SFT uses the relation between the transverse and longitudinal components of residual stress in the rail to separate out the applied stress (or the rail neutral temperature). A field test for this experiment showed that the RNT calculated by MAPS-SFT was within 5°C from the strain gauges technique, which can be considered to be acceptable. The disadvantage of this technique is that this system

needs to be calibrated on an unstressed rail before taking the measurements. Hence, a sample rail of the same type of the rail in the field is needed.

There are several techniques that researchers have developed to determine applied stress in specimens. Egle and Bray (1979) developed an ultrasonic probe that generates and detects longitudinal waves propagating along the rail for stress measurement. The measurement of the travel time of the waves was done by using a pulse overlay technique. The field test showed that the probe was capable of measuring longitudinal stress changes at specific locations in rail with an accuracy of $\pm$ 7 MPa. Bray and Leon (1985) utilized a technique for longitudinal force measurement by using head-waves (L_{CR}) to measure the travel time changes caused by stress changes. This technique measures bulk stresses instead of surface stresses. The travel time was taken at different locations and these data were averaged to establish a zero-force travel time.

Material texture has a significant effect on wave propagation. There are various ways to accommodate this texture effect. One of them is to take the measurements at various locations to obtain an average wave speed, which is independent of the texture. Bray (2002) used an L_{CR} technique to identify the changes in stress in pressure vessels, piping, and welds. The measurements were taken at different locations with the probe oriented in the same direction to establish a base line travel time where the texture effects are constants.

Husson et al. (1982) developed a method for measuring surface residual stresses using the acoustoelasticity of Rayleigh wave. An edge bond transducer was used for Rayleigh wave generation, and two electromagnetic transducers (EMATS) were used for

detection of the Rayleigh wave. A calibration experiment was first performed to obtain the acoustoelastic coefficient. Using this calibration measurement results and the measurement of the variation of the Rayleigh wave velocities from the two EMATS, the surface residual stress were calculated. Duquennoy et al. (1999) determined the stress distribution along aluminum alloy sheets using Rayleigh waves. A wedge transducer working at a frequency of 2.25 MHz was used to generate the Rayleigh waves. The relative change of the Rayleigh wave velocities were calculated from the relative change of the time of flight, and the residual stress profile were obtained by this method. The results from this method were compared to the results obtained from a destructive method, and both of the results were similar.

The proposed method utilizes a non-destructive measurement technique that is not labor intensive by using a polarization of Rayleigh waves. A wedge transducer will be used to generate the Rayleigh wave. The change in the polarization of the Rayleigh wave is measured instead of the wave speed; therefore, information on the propagation distance is not needed (Junge, 2003). This technique is also applicable on rails under tension or compression. Successful completion of this technique would allow for a development in a non-contact measurement method by using a pulse-laser instead of wedge transducer to generate the Rayleigh wave.

2.2 Acoustoelastic Effect

Acoustoelastic effect or acoustoelasticity is defined as the dependency of ultrasonic wave speed on stress. The determination of material properties such as

material constants, flaw detection, or applied stress can be obtained by various types of ultrasonic waves (Crecraft, 1962). Crecraft's research found that the acoustoelastic effect is a functional technique for determining material properties.

Murnaghan (1951) developed a nonlinear elastic theory for isotropic materials. This theory introduces third-order elastic (TOE) constants, *l*, *m*, and *n* for an isotropic body, which help to explain the acoustoelastic effect with a theoretical model. The theory was applied by Toupin and Berstein (1961) to a deformed perfectly elastic material to observe the propagation behavior of acoustic waves. Pao and Garmer (1985) extended this theory to an orthotropic elastic solid.

The acoustoelastic effect is very small. Special techniques are required to measure the stress-induced velocity changes. Crecraft (1967) used the sing-around technique to measure the acoustoelastic effect. This technique uses two transducers that are coupled to the specimen. The first transducer generates a pulse to be received by the second transducer. This pulse is then used to retrigger the sending transducer. The frequency of this echoing pulse is related to the travel time of the ultrasonic wave.

Hughes and Kelly (1953) utilized Murnaghan's theory to derive the expressions for the velocities of elastic waves in a stressed solid. The transmission time of elastic pulses through the solid was measured to determine the velocities of longitudinal and shear waves as a function of applied stress. The specimens used in the test were polystyrene, iron, and Pyrex glass.

Hirao et al. (1981) conducted a research on the acoustoelastic effect on Rayleigh waves in a homogeneous isotropic material. The experiment was performed on mild steel samples using a sing-around technique under uniform stress and non-uniform stress distribution. The results show that under a non-uniform stress, Rayleigh wave becomes dispersive under a low frequency, and the dispersion attenuates as the frequency increases. Under uniform stress distribution, Rayleigh waves are non-dispersive and the velocity change is linear with the change in stress. Gokhale (2007) found that the acoustoelastic effect of Rayleigh waves in rail steel is more promising than those of the longitudinal, shear, and Lamb waves.

Egle and Bray (1976) measured the acoustoelastic effect and third-order constants for rail steel. The experiment was conducted by using ultrasonic transducers with center frequencies of 2.5 MHz and 5 MHz. The transducers were coupled to the specimen for generation and detection of longitudinal waves. The acoustoelastic constants were determined from the measurement of the change in wave speeds in five directions under uniaxial stress, and the results showed a consistency with the prediction of the second order theory by Hughes and Kelly (1953).

Hurlebaus and Jacobs (2006) developed a dual-probe interferometer to enable two independent (uncoupled) detection probes. The robustness of this dual-probe interferometer was demonstrated by measuring the same Lamb waves at two different locations with the same propagation distance in an aluminum plate. This system has advantages of simultaneously measuring two independent simultaneous measurements and reducing the number of optical components.

Some of the techniques described in this section identify the wave velocities using the propagation time of ultrasonic waves. The limitation of using these techniques is that the influence of material properties is accumulated along the path of wave propagation. Also, an exact propagation distance is required to calculate the velocity of the waves. The method used in this thesis uses a point-wise measurement, and it does not have the disadvantages of being integral (accumulation of material properties along the path of wave propagation) and non reference-free. This method utilizes the acoustoelasticity of Rayleigh waves. Fig. 2.3 shows the change of Rayleigh wave polarization with applied stress.

Out-of-plane component

$\sigma > 0$

In-plane component

$\sigma = 0$
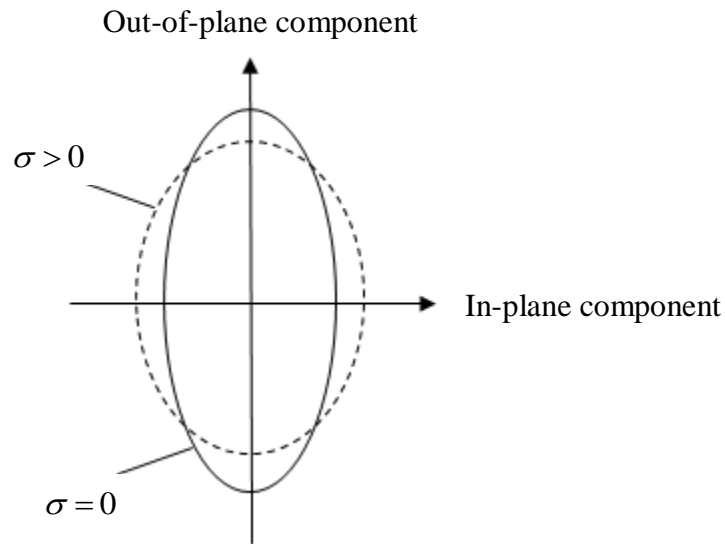
Fig. 2.3 – Change of Rayleigh wave polarization under applied stress

CHAPTER III

THEORETICAL BACKGROUND

This chapter provides descriptions on the subject of Rayleigh waves, the acoustoelastic effect, the equation of motion, and third-order constant (TOE). These subjects help in understanding the analytical model discussed in the next chapter.

3.1 Wave Propagation

The equation of motion of an elastic solid is governed by the Lame-Navier equation given by

$$\frac{\partial T_{mn}}{\partial x_n} + \rho f_m = \rho \frac{\partial^2 u_m}{\partial t^2} \ , \tag{3.1}$$

where ρ symbolizes the density of the material, f_m are the internal body forces, x_n denotes the direction in the coordinate system shown in Fig. 3.1, u_m is the displacement in the x_m direction, and T_{mn} denotes the stress tensor in the generalized Hooke's Law given as

$$T_{mn} = C_{mnpq} \frac{\partial u_p}{\partial x_q} \ . \tag{3.2}$$

By substituting Eq. (3.2) to Eq. (3.1) and neglecting the body forces, the equation of motion can be written as

$$C_{mnpq} \frac{\partial^2 u_p}{\partial x_n \partial x_q} = \rho \frac{\partial^2 u_m}{\partial t^2} \quad , \tag{3.3}$$

where C_{mnpq} is the second order stiffness tensor given by

$$C_{mnpq} = \lambda \delta_{mn} \delta_{pq} + \mu(\delta_{mp}\delta_{nq} + \delta_{mq}\delta_{nq}) \ . \tag{3.4}$$

Notation λ and μ in Eq. (3.4) denote the Lame's constants, and δ is the Kronecker delta. Lame's constants can be expressed in terms of Young's Modulus E, and Poisson's ratio υ

$$\mu = \frac{E}{2(1+\upsilon)}, \qquad \text{and} \qquad \lambda = \frac{E\upsilon}{(1+\upsilon)(1-2\upsilon)} \ . \tag{3.5}$$

By plugging Eq. (3.4) into Eq. (3.3), the equation of motion is now simplified into

$$\mu \nabla^2 u_m + (\lambda + \mu) \frac{\partial}{\partial x_m} \left(\frac{\partial u_n}{\partial x_n} \right) = \rho \frac{\partial^2 u_m}{\partial t^2} , \tag{3.6}$$

where ∇ denotes the nabla operator $\nabla^2 = \frac{\partial^2}{\partial x_1^2} + \frac{\partial^2}{\partial x_2^2} + \frac{\partial^2}{\partial x_3^2}$.
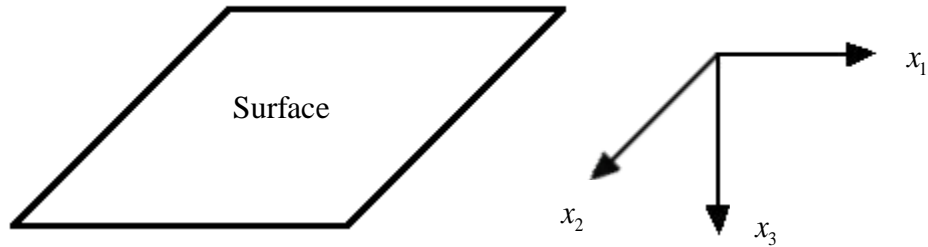
Fig. 3.1 – Coordinate system

To satisfy the equation of motion in Eq. (3.6), the displacement vector can be expressed in the form of

$$\boldsymbol{u} = f(\boldsymbol{x} \cdot \boldsymbol{p} - ct)\boldsymbol{d} \, , \tag{3.7}$$

where c is the wave speed, $\boldsymbol{p}$ represents the unit propagation, $\boldsymbol{x}$ is the location of the displacement vector, and $\boldsymbol{d}$ is the unit displacement vectors.

Longitudinal waves have polarization vectors parallel to the displacement vector, or $\boldsymbol{p} = \boldsymbol{d}$. Conversely, shear waves have polarization vector perpendicular to the displacement vector, or $\boldsymbol{p} \cdot \boldsymbol{d} = 0$. By inserting each of these characteristics into Eq. (3.7) and then plugging the result into Eq. (3.6), the wave speed can be determined as

$$c_l^2 = \frac{\lambda + 2\mu}{\rho} \, , \tag{3.8}$$

$$c_S^2 = \frac{\mu}{\rho} \, , \tag{3.9}$$

where c_l and c_S are the longitudinal wave speed and the shear wave speed, respectively.

Eq. (3.7) can be uncoupled in terms of longitudinal and shear waves by utilizing the Helmholtz decomposition. The displacement in uncoupled terms can be expressed in terms of a scalar function ϕ and a vector field $\boldsymbol{\psi}$

$$\boldsymbol{u} = \nabla\phi + \nabla \times \boldsymbol{\psi} \, . \tag{3.10}$$

By substituting Eq. (3.10) back into Eq. (3.6), the uncoupled equations are

$$\nabla^2 \phi = \frac{1}{c_l^2} \frac{\partial^2 \phi}{\partial t^2} \qquad \text{and} \qquad \nabla^2 \psi = \frac{1}{c_s^2} \frac{\partial^2 \psi}{\partial t^2} \quad . \tag{3.11}$$

3.2 Rayleigh Wave

A Rayleigh wave is a non dispersive wave that propagates on the free surface of a solid. It was first found by Lord Rayleigh in 1885. The particles of a Rayleigh wave travel in a counterclockwise direction with an elliptic trajectory along the free surface and then change to a clockwise direction as the depth increases. A Rayleigh wave's amplitude decays as a function of depth (coordinate x_3), and the motion does not depend on the coordinate x_2. Fig. 3.2 shows the trajectory plot of a Rayleigh wave particle.

3.2.1 Rayleigh Wave Speed

In Rayleigh waves, the scalar function and vector field can be assumed to be

$$\phi = F(x_3)e^{ik(x_1-ct)}$$

$$\psi = G(x_3)e^{ik(x_1-ct)} \tag{3.12}$$

where F and G are functions of x_3, and k is the wave number given by $k = 2\pi/\lambda$. Plugging Eq. (3.12) into Eq. (3.11) gives the surface wave motion

$$\phi = A_1 e^{-kqx_3} e^{ik(x_1-ct)}$$

$$\psi = B_1 e^{-ksx_3} e^{ik(x_1-ct)}, \tag{3.13}$$

where A_1 and B_1 are arbitrary constants and

$$q = \sqrt{1 - \left(\frac{c_R}{c_l}\right)^2} \qquad\qquad s = \sqrt{1 - \left(\frac{c_R}{c_s}\right)^2} \ .$$

The boundary conditions require that stress is equal to zero at $x_3 = 0$. Substitution of this boundary condition into Eq. (3.13) yields the Rayleigh characteristic equation

$$\left(2 - \frac{c_R^2}{c_s^2}\right)^2 - 4\sqrt{\left(1 - \frac{c_R^2}{c_l^2}\right)}\sqrt{\left(1 - \frac{c_R^2}{c_s^2}\right)} = 0 \ . \qquad (3.14)$$
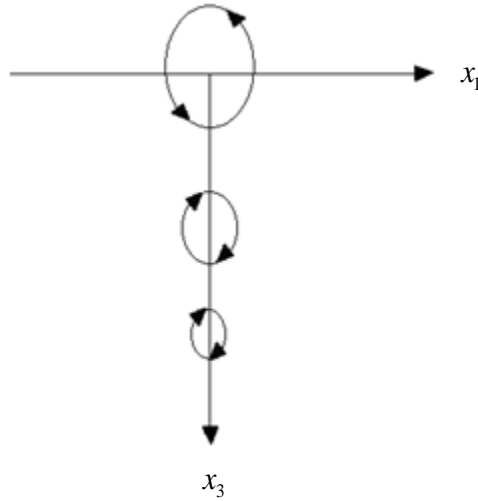
Fig. 3.2 – Trajectory plot for various depths (*Junge, 2003*)

Eq. (3.14) has six roots, whose values depend only on Poisson's ratio υ for a given elastic media. Victorov (1966) showed that for arbitrary values of υ corresponding to real media ($0 < \upsilon < 0.5$), Eq. (3.14) has only one such root. An approximate expression for the Rayleigh wave velocity c_R is given by Graff (1991)

$$\frac{c_R}{c_S} = \frac{0.87 + 1.12\upsilon}{1+\upsilon} \ .$$

(3.15)

This propagation velocity is smaller than those of the body waves. As the velocity c_R is independent of the wavelength, the wave propagation is non dispersive. The propagation of a Rayleigh wave is depicted in Fig. 3.2. It can be shown that an arbitrary point will move with elliptical motion as the Rayleigh wave passes by. Most of the energy in the Rayleigh wave is present in the depth of one wavelength from the surface. Due to this skin effect, the Rayleigh wave has great potential for detection of faults at the surface of structures. Furthermore, the Rayleigh wave causes the most damage during an earthquake because it carries more energy at the surface than either longitudinal or shear waves.

3.2.2 Polarization of Rayleigh Wave

Rose (1999) derived the displacements of the Rayleigh waves that satisfy the boundary conditions to be

$$
\begin{aligned}
u_1 &= A(re^{-kqx_3} - 2sqe^{-ksx_3})e^{ik(x_1 - c_R t)} \\
u_3 &= iAq(re^{-kqx_3} - 2e^{-ksx_3})e^{ik(x_1 - c_R t)}
\end{aligned}
$$

(3.16)

,

where $r = 2 - (c_R / c_S)^2$ and $A = kB_1 / 2q$. Plotting the displacement of u_1 and u_3 gives the ellipse shape of the particle motion. Polarization of a Rayleigh wave can be described as the ratio of maximum displacements along the ellipse's axes given by

$$\Pi = \frac{u_1}{u_3} \ .$$

(3.17)

3.3 Lamb Waves

Consider a double-bounded medium that has two parallel surfaces in close proximity. Disturbances are constrained to move between the two surfaces, and therefore the system behaves as a waveguide. Of interest is the case where the top and bottom surfaces are traction-free. For this set of boundary conditions, waves known as Lamb waves propagate in the plate. Depicted in Fig. 3.3 are the displacement profiles for the first Lamb modes. The essence of the analysis is that standing waves are established in the transverse direction, while propagating waves travel in the lengthwise direction. Consider a plane, harmonic Lamb wave propagating along the positive x_1-direction in a plate with thickness h. The scalar and vector potentials can be expressed as

$$\phi = \left[C_1 \sin\left(\sqrt{k^2 - k_L^2}\, x_3 \right) + C_2 \cos\left(\sqrt{k2 - k_L^2}\, x_3 \right) \right] e^{ik(x_1 - ct)} \tag{3.18}$$

$$\psi = \left[D_1 \sin\left(\sqrt{k^2 - k_S^2}\, x_3 \right) + D_2 \cos\left(\sqrt{k2 - k_S^2}\, x_3 \right) \right] e^{ik(x_1 - ct)}, \tag{3.19}$$

where k_L and k_S are the wave numbers of the longitudinal and shear waves, respectively, C_1, C_2, D_1 and D_2 are arbitrary constant. Implementation of the boundary conditions $\sigma_{33} = \sigma_{13} = 0$ at the free surface $x_3 = \pm h/2$ leads, after some manipulation, to the well-known Rayleigh-Lamb frequency equations

$$\frac{\tanh\left(\dfrac{h}{2} \sqrt{k^2 - k_S^2} \right)}{\tanh\left(\dfrac{h}{2} \sqrt{k^2 - k_L^2} \right)} = - \frac{4k^2 \sqrt{k^2 - k_S^2} \sqrt{k^2 - k_L^2}}{(2k^2 - k_S^2)^2} \tag{3.20}$$

for the symmetric case and

$$\frac{\tanh\left(\dfrac{h}{2}\sqrt{k^2 - k_S^2}\right)}{\tanh\left(\dfrac{h}{2}\sqrt{k^2 - k_L^2}\right)} = -\frac{(2k^2 - k_S^2)^2}{4k^2\sqrt{k^2 - k_S^2}\sqrt{k^2 - k_L^2}} \tag{3.21}$$

for the antisymmetric case. For the symmetric mode shapes, the displacement u_1 is symmetric about the axis $x_3 = 0$; and for the antisymmetric mode shapes the displacement u_1 is antisymmetric about the axis $x_3 = 0$ (Fig. 3.3). At a spatially-fixed plate cross section, the amplitude of a mode shape will oscillate with angular frequency ω as wavefronts travel through the cross-section with velocity c. Eq. (3.20) and Eq. (3.21) can be expressed in terms of ω and c using the relationship $k = \omega / c$.
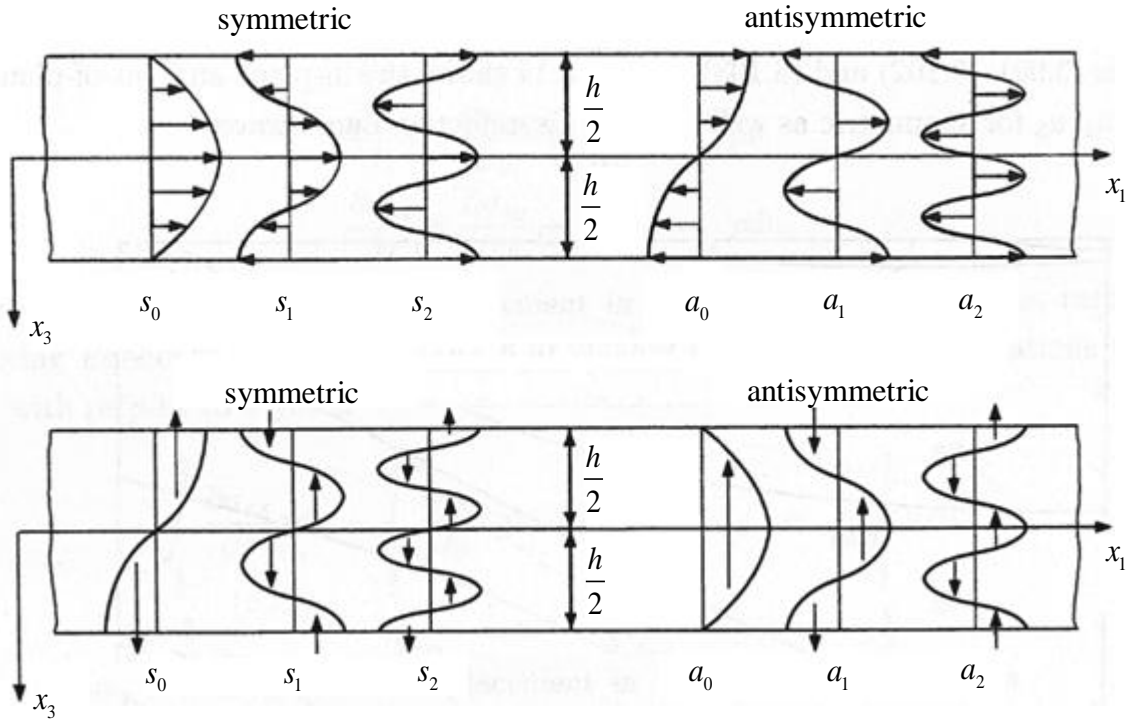
Fig. 3.3 – Symmetric and antisymmetric components of the u_1, u_3 displacements (*Hurlebaus, 2005*)

For a given frequency, these equations can be solved for the unknown velocity of the mode in question. A plot of ω vs. c (or ω vs. k) for a particular mode is known as a dispersion curve. Fig. 3.4 shows typical dispersion curves in the normalized (ω, k) domain for Lamb waves together with dispersion curves for the longitudinal and shear wave. The symmetric Lamb modes are called $s_0, s_1, s_2, ...$ and the antisymmetric modes are called $a_0, a_1, a_2, ...$. Lamb waves are – as opposed to Rayleigh waves – dispersive, whereby the propagation velocity of a specific Lamb mode depends upon its oscillation frequency. For a given (ω, k) combination, the mode shape can be computed using Eq. (3.10), Eq. (3.18), and Eq. (3.19). Fig. 3.3 shows the in-plane and out-of-plane displacements u_1, u_3 for symmetric as well as for antisymmetric Lamb waves (Hurlebaus, 2005).

3.4 States of a Solid Body

Natural, initial, and final states are different states that can be found in a solid. A solid body is in the *natural state* when there is no residual stress and strain in the body. In practice, such state does not exist in a solid material. Solid materials experience stresses from fabrication processes or external loading that leads to deformation. When material undergoes such stress, it is said to be in its *initial state.* The *final state* takes place when the material undergoes additional deformation due to other stress applied on the body such as the propagation of ultrasonic wave. Fig. 3.5 shows the arrangement of the three states of a body in the Cartesian coordinate system.
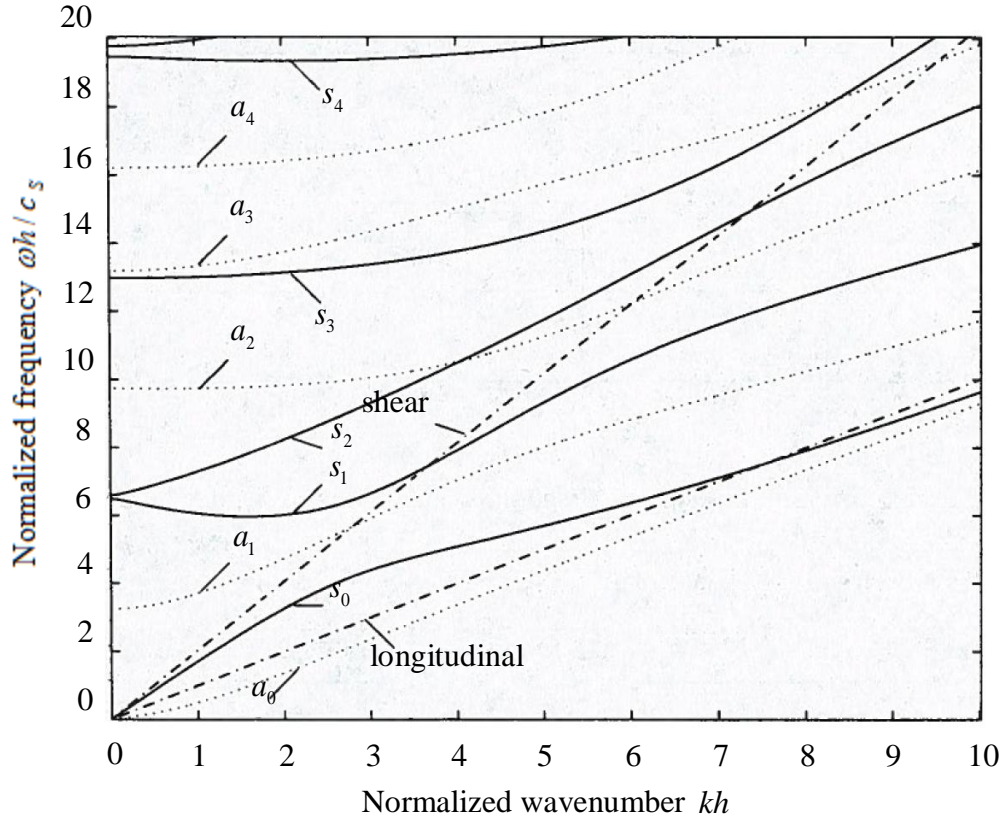
Fig. 3.4 – Theoretical dispersion curves calculated from Rayleigh-Lamb frequency equations (*Hurlebaus, 2005*)

Pao et al. (1984) refers the position vectors of the natural, initial, and final states to be $\boldsymbol{\xi}$, $\boldsymbol{X}$, and $\boldsymbol{x}$ respectively. The relationship of the displacements of these states can be expressed as

$$\boldsymbol{u}^i(\boldsymbol{\xi}) = \boldsymbol{X} - \boldsymbol{\xi} \tag{3.22}$$

$$\boldsymbol{u}^f(\boldsymbol{\xi}) = \boldsymbol{x} - \boldsymbol{\xi} \tag{3.23}$$

$$\boldsymbol{u}(\boldsymbol{\xi}) = \boldsymbol{x} - \boldsymbol{X} = \boldsymbol{u}^f - \boldsymbol{u}^i \quad , \tag{3.24}$$

where superscript i and f stand for initial and final, respectively.
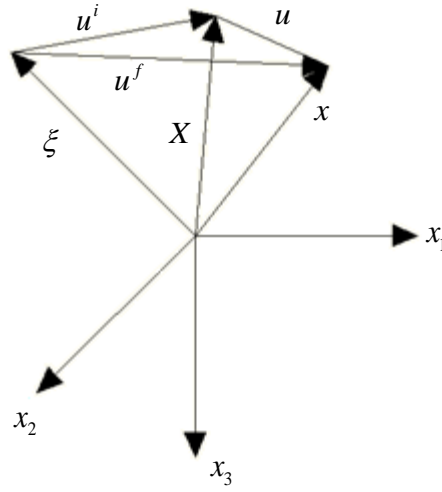
Fig. 3.5 – Coordinate system of natural, initial, and final states of a body (*Junge, 2003*)

3.5 Third-Order Elastic (TOE) Constant

The existence of elastic constants is very important in determining the stress state of the material using the ultrasonic wave method. The second order elastic constant can be found by using the linear theory of elasticity. When there is an applied stress in the material, the second order elastic constants cannot explain the change in ultrasonic wave velocities. Thus, a higher order of nonlinear elasticity theory was established. This theory introduces the second-order Lame constant and the third-order elastic constant. For isotropic materials, the second- and third-order elastic constants can be expressed in the forms

$$C_{\alpha\beta\gamma\delta} = \lambda\delta_{\alpha\beta}\delta_{\gamma\delta} + \mu(\delta_{\alpha\gamma}\delta_{\beta\delta} + \delta_{\alpha\delta}\delta_{\beta\gamma}), \tag{3.25}$$

and

$$
\begin{aligned}
C_{\alpha\beta\gamma\delta\varepsilon\eta} = {}& \upsilon_1 \delta_{\alpha\beta}\delta_{\gamma\delta}\delta_{\varepsilon\eta} + \upsilon_2 [\delta_{\alpha\beta}(\delta_{\gamma\varepsilon}\delta_{\delta\eta} + \delta_{\gamma\eta}\delta_{\delta\varepsilon}) + \delta_{\gamma\delta}(\delta_{\alpha\varepsilon}\delta_{\beta\eta} + \delta_{\beta\varepsilon}\delta_{\alpha\eta}) + \\
& \delta_{\varepsilon\eta}(\delta_{\alpha\gamma}\delta_{\beta\delta} + \delta_{\alpha\delta}\delta_{\beta\gamma})] + \upsilon_3[\delta_{\alpha\gamma}(\delta_{\beta\varepsilon}\delta_{\delta\eta} + \delta_{\beta\eta}\delta_{\delta\varepsilon}) + \\
& \delta_{\beta\delta}(\delta_{\alpha\varepsilon}\delta_{\gamma\eta} + \delta_{\alpha\eta}\delta_{\gamma\varepsilon}) + \delta_{\alpha\delta}(\delta_{\beta\varepsilon}\delta_{\gamma\eta} + \delta_{\beta\eta}\delta_{\gamma\varepsilon}) + \\
& \delta_{\beta\gamma}(\delta_{\alpha\varepsilon}\delta_{\delta\eta} + \delta_{\alpha\eta}\delta_{\delta\varepsilon})],
\end{aligned}
\tag{3.26}
$$

where υ_1, υ_2, and υ_3 are the Toupin and Bernstein (1961) notation of TOE.

CHAPTER IV

ANALYTICAL MODEL

This chapter describes the analytical model that explains the polarization of Rayleigh waves. This model consists of an equation of motion for pre-stressed bodies and the relation between polarization and residual stress.

4.1 Equation of Motion for a Pre-stressed Body

The state of stress at a given point as a function of X is defined by the Cauchy stress tensor, $t^i(X)$. While the Piola-Kirchhoff stress tensor, $T^i(\xi)$, describes the state of stress at the same given point in the natural configuration. Both of these tensors are related by

$$t^i_{JK} = \left|\frac{\partial X}{\partial \xi}\right|^{-1} \frac{\partial X_K}{\partial \xi_\beta} \frac{\partial X_J}{\partial \xi_\alpha} T^i_{\alpha\beta} \quad . \tag{4.1}$$

The relation of the final state of stress of these two tensors can also be found by using the same analogy given by

$$t^f_{ij} = \left|\frac{\partial x}{\partial \xi}\right|^{-1} \frac{\partial x_i}{\partial \xi_\alpha} \frac{\partial x_j}{\partial \xi_\beta} T^f_{\alpha\beta} = \left|\frac{\partial x}{\partial X}\right|^{-1} \frac{\partial x_i}{\partial \xi_K} \frac{\partial x_j}{\partial \xi_L} T^f_{KL} \quad , \tag{4.2}$$

and the stress change from the initial to final state is defined by

$$T_{JK} = T^f_{JK} - t^i_{JK}$$

$$T_{\alpha\beta} = T^f_{\alpha\beta} - t^i_{\alpha\beta}. \tag{4.3}$$

Given these basic explanations, Pao et al. (1984) derives the equation of motion as

$$\frac{\partial}{\partial X_J}\left[(\delta_{IK}t^i_{JL} + \hat{C}_{IJKL})\frac{\partial u_K}{\partial X_L}\right] = \rho^0(1-\varepsilon^i_{NN})\frac{\partial^2 u_i}{\partial t^2}, \tag{4.4}$$

where $\hat{C}_{IJKL}$ represents the adapted stress tensor of a pre-stressed body. Both adapted stress tensor and initial strain are respectively given by

$$\begin{aligned}\hat{C}_{IJKL} = {}& \lambda\delta_{IJ}\delta_{KL} + \mu(\delta_{IK}\delta_{JL} + \delta_{IL}\delta_{JK}) + [(-\lambda + \upsilon_1)\delta_{IJ}\delta_{KL} + \\ & (-\mu + \upsilon_2)(\delta_{IK}\delta_{JL} + \delta_{IL}\delta_{JK})]\varepsilon^i_{MM} + 2(\lambda + \upsilon_2)(\varepsilon^i_{IJ}\delta_{KL} + \varepsilon^i_{KL}\delta_{IJ}) + \\ & 2(\mu + \upsilon_3)(\varepsilon^i_{IK}\delta_{JL} + \varepsilon^i_{IL}\delta_{JK} + \varepsilon^i_{JK}\delta_{IL} + \varepsilon^i_{JL}\delta_{IK})\end{aligned} \tag{4.5}$$

and the initial strain, ε^i_{KL}, is determined by

$$\varepsilon^i_{KL} = \frac{-\lambda}{2\mu(3\lambda + 2\mu)}\delta_{KL}t^i_{NN} + \frac{1}{2\mu}t^i_{KL}. \tag{4.6}$$

4.2 Rayleigh Waves in Pre-stressed Bodies

Assuming that the initial stress is homogeneous, Eq. (4.4) can be simplified into

$$(\delta_{IK}t^i_{JL} + \hat{C}_{IJKL})\frac{\partial u_K}{\partial X_J X_L} = \rho(1-\varepsilon^i_{NN})\frac{\partial^2 u_I}{\partial t^2}. \tag{4.7}$$

In this chapter, the displacement field is selected to be in the form

$$\boldsymbol{u} = \boldsymbol{a}e^{ik(X_1 + pX_3 - c_R t)}, \tag{4.8}$$

where $\boldsymbol{a}$ represents the displacement vector, and p is the decay parameter. The form of this displacement field represents the propagation of a Rayleigh wave where its motion decays exponentially with increasing depth. Plugging Eq. (4.8) into Eq. (4.7) yields the equation

$$\{p^2\hat{\boldsymbol{S}} + p(\hat{\boldsymbol{R}} + \hat{\boldsymbol{R}}^T) + \hat{\boldsymbol{Q}} - \rho_0(1 - \varepsilon_{NN}^i)c_R^2\boldsymbol{I}\}\boldsymbol{a} = 0,$$

or

$$\{\boldsymbol{D}(c_R, p)\}\boldsymbol{a} = 0, \tag{4.9}$$

where $\boldsymbol{I}$ is the identity matrix, and $\hat{\boldsymbol{S}}$, $\hat{\boldsymbol{R}}$, and $\hat{\boldsymbol{Q}}$ are given by

$$\hat{S}_{IK} = \hat{C}_{I3K3} \qquad \hat{R}_{IK} = \hat{C}_{I1K3} \qquad \hat{Q}_{IK} = \hat{C}_{I1K1} + \delta_{IK}t_{11}^i. \tag{4.10}$$

The displacement vector $\boldsymbol{a}$ can be determined by solving for null space of $\boldsymbol{D}$ for each p_i, which can be solved by setting

$$\|\boldsymbol{D}(c_R, p)\| = 0 . \tag{4.11}$$

The decay parameters, p_i, solved in Eq. (4.11) consist of three pairs of complex conjugate roots for p. Once the displacement vectors $\boldsymbol{a}_i$ are determined, the displacement field can be written as a linear combination of the single solutions using the matrix notation

$$\boldsymbol{u} = \boldsymbol{A}\boldsymbol{G}(X_3)\boldsymbol{f}e^{ik(X_1 - ct)}, \tag{4.12}$$

where f is a vector that consists of factors for the linear combination, $A = [a_1, a_2, a_3]$, and

$$G(X_3) = \begin{bmatrix} e^{ikp_1 X_3} & 0 & 0 \\ 0 & e^{ikp_2 X_3} & 0 \\ 0 & 0 & e^{ikp_3 X_3} \end{bmatrix}. \qquad (4.13)$$

The boundary condition of the state of stress for Rayleigh waves in a pre-stressed body is given by

$$T_{12} = \hat{C}_{I2KL} \frac{\partial u_K}{\partial X_L} = 0 \text{ , at } X_3 = 0 \text{ .} \qquad (4.14)$$

Plugging Eq. (4.12) into the boundary condition yields

$$(\hat{R}^T A + \hat{S} A P) f = 0,$$

or

$$\big(B(c_R, p)\big) f = 0 \text{ ,} \qquad (4.15)$$

where

$$P = \begin{bmatrix} p_1 & 0 & 0 \\ 0 & p_2 & 0 \\ 0 & 0 & p_3 \end{bmatrix}. \qquad (4.16)$$

For a non-trivial solution of Eq. (4.15), the matrix B must equal to zero or

$$\big\| B(c_R, p) \big\| = 0 \text{ ,} \qquad (4.17)$$

and the vector f can be found by solving for the null-space of B.

The polarization of Rayleigh waves is defined as the ratio of maximum displacements in the x_1 and x_3 directions on the free surface. The polarization of Rayleigh wave is given by

$$\Pi = \frac{(\boldsymbol{Af})_1}{(\boldsymbol{Af})_2} \ . \tag{4.18}$$

CHAPTER V

NUMERICAL SIMULATION

This chapter provides the numerical solution to the propagation of Rayleigh waves through rail steel. The iterative algorithm for numerical simulation is presented first, followed by the simulation results and frequency range.

5.1 Algorithm for Numerical Simulation

The numerical simulation to the problem of Rayleigh wave propagation is done by using Matlab software. This simulation determines the changes of Rayleigh wave speed, c_R, and polarization of the Rayleigh wave, $\Delta\Pi$, on residual stresses. Junge (2003) has arranged the iterative algorithm as follows

1. Identify an initial Rayleigh wave speed, c_{R0}. This can be done by using Eq. (3.14). The longitudinal and shear wave speeds can be determined by using Eq. (3.8) and Eq. (3.9). Poisson's ratio is needed to perform this calculation, and it can be found by

$$\upsilon = \frac{\lambda}{2(\lambda + \mu)} \quad .$$

(5.1)

2. Plug in the wave speed from step 1 into Eq. (4.9) and solve for p_i that makes the determinant of $\boldsymbol{D}$ equal to zero.

3. For each value of p_i, solve for the null-space, $\boldsymbol{a}_i$, in Eq. (4.9) and construct the matrix $\boldsymbol{A}$.

4. Use the values of p to construct the matrix $\boldsymbol{P}$ in Eq. (4.15).

5. Construct matrix $\boldsymbol{B}$ as stated in Eq. (4.14).

6. If the determinant of matrix $\boldsymbol{B}$ is not equal to zero, use another value of c_{R0} and start all over again from step 2.

7. The value of c_{R0} that satisfies the boundary condition is the Rayleigh wave speed, c_R, on the residual stress.

8. Solve for the null-space, f, in Eq. (4.14)

9. Compute the polarization vector using Eq. (4.17)

5.2 Simulation Results

This section discusses the influence of applied stress to the relative change of Rayleigh wave speed and Rayleigh wave polarization. A sensitivity analysis is done to examine how the uncertainties in the TOE constants affect the Rayleigh wave speed and polarization. A trajectory plot of particle motion for unstressed and stressed rail is illustrated using the numerically predicted Rayleigh wave polarization.

5.2.1 Relative Change of Rayleigh Waves on Residual Stress

The relative change of the Rayleigh wave speed and polarization with stress are very small in rail steel. To identify them, proportionality constants are introduced. These constants are defined as a relative change in Rayleigh wave speed and polarization over the applied stress. The relative change of Rayleigh wave speed is given by

$$\Delta c_R = \frac{c_R - c_{R0}}{c_{R0}} \quad , \tag{5.2}$$

and the relative change of Rayleigh wave polarization is

$$\Delta \Pi = \frac{\Pi - \Pi_0}{\Pi_0} \quad . \tag{5.3}$$

The numerical simulation in this chapter uses the properties of rail steel found by Egle and Bray (1976) as shown in Table 5.1.

Table 5.1 – Material properties of rail steel

ρ (kg/m^3)	λ (GPa)	μ (GPa)	υ_1 (GPa)	υ_2 (GPa)	υ_3 (GPa)
7799	110.7	82.4	-96	-254	-181

Rail steel has a yield strength of 450 MPa. Therefore, this simulation ranges from a compressive force of -440 MPa to a tensile force of 440 MPa. Fig. 5.1(top) shows the results of the simulation on the change of wave speed on residual stress. This plot shows that there is a linear relation between them and is given by

$$\Delta c_R = k^c \cdot t_{11}^i \quad , \tag{5.4}$$

where k^c is a wave speed proportionality factor. Similarly, Fig. 5.1(bottom) also shows that there is linear relation between $\Delta \prod$ and t_{11}^i given by

$$\Delta \prod = k^p \cdot t_{11}^i \quad , \qquad\qquad (5.5)$$

where k^p is the polarization proportionality factor. Both values of k^c and k^p are used to measure the sensitivity of the Rayleigh wave speed and the polarization of the Rayleigh wave, respectively. Based on the simulations, the proportionality factors are determined to be

$$k^c = \text{-4.3 x } 10^{-7} / \text{MPa} \qquad \text{and} \qquad k^p = 9.8 \text{ x } 10^{-6} / \text{MPa} \, .$$

The value of k^p is greater than the value of k^c by approximately one order of magnitude. This shows that the change of Rayleigh wave polarization on residual stress is higher than the change of wave speed; thus, it is easier to be analyzed.
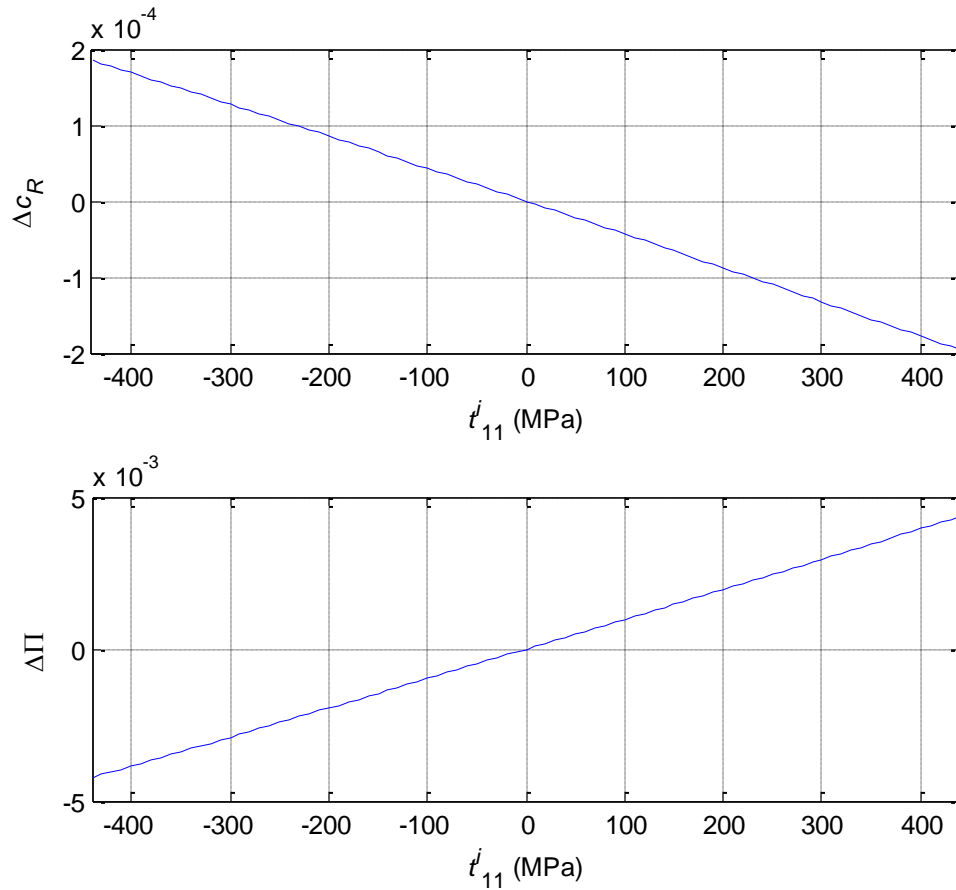
Fig. 5.1 – The change in wave speed (top) and the change in Rayleigh wave polarization (bottom) on residual stress for rail steel

5.2.2 Sensitivity Analysis

In the previous section, TOE constants are assumed to remain unchanged in the simulation. In reality, the values of TOE constants have some uncertainties. Eagle and Bray (1976) identified an estimated error of the TOE constants for rail steel to be about 3% - 4%. Smith et al. (1966) found the uncertainties of TOE constants for austenitic Steel Hecla ATV to be more than 20%. A sensitivity analysis on the TOE constants is necessary to discover the change of wave speed and polarization of Rayleigh waves

against uncertainties of TOE constants. In contrast, Lame constants can be determined precisely and, hence, can be assumed to remain constant.

Assuming an uncertainty of 20% in rail steel properties, the scale of relative change of Rayleigh wave speed and polarization of Rayleigh wave can be seen in Fig. 5.2. This plot shows that the experimental results may vary within the shaded area since the values of TOE constants are not known exactly.

The proportionality factors are investigated in this sensitivity analysis to have a better understanding of the uncertainties in TOE constants. Table 5.2 shows the percentage differences of maximum and minimum proportionality factors to the real value for an uncertainty of 20%. The percentage difference of k^p is much smaller than k^c against uncertainties, meaning that the Rayleigh wave polarization is more robust than the Rayleigh wave speed.
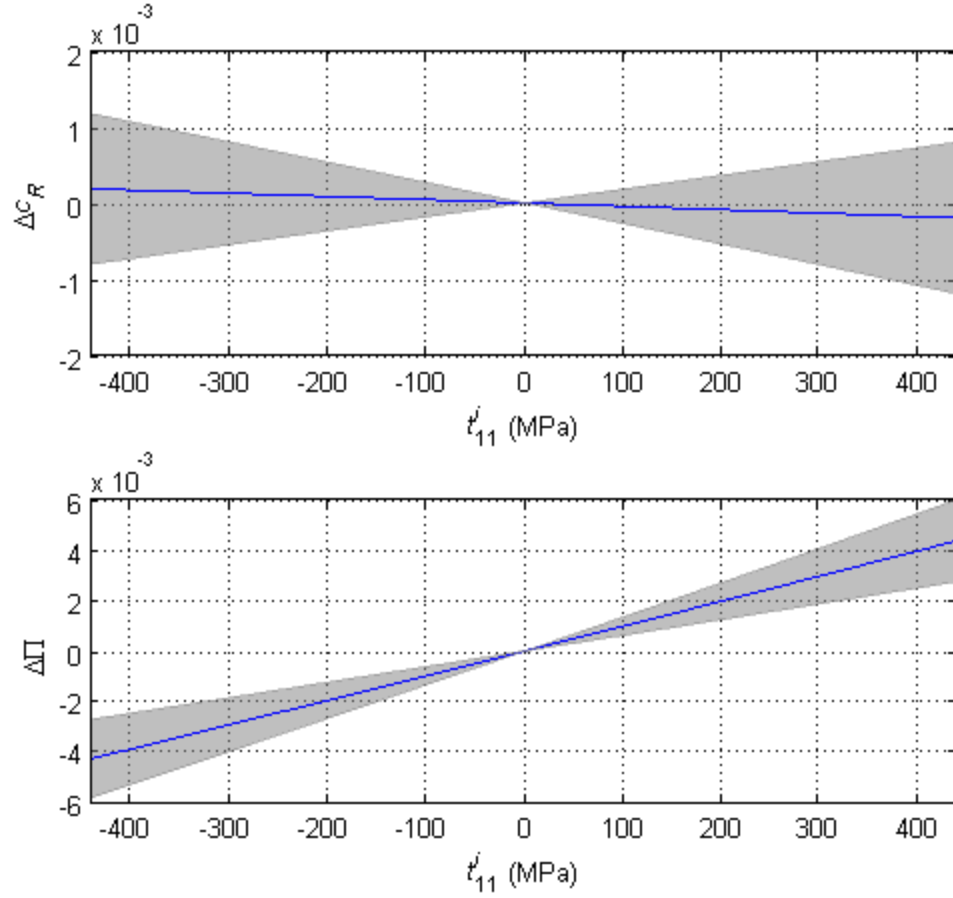
Fig. 5.2 – The change in wave speed (top) and the change in Rayleigh wave polarization (bottom) against uncertainties. The changes are within the shaded area.

In Section 5.2.1, the change in Rayleigh wave polarization on residual stress proves to be higher than the change of Rayleigh wave speed. Thus, Rayleigh wave polarization is more sensitive to stress than the Rayleigh wave speed. In addition, the Rayleigh wave polarization is more robust against the uncertainties of rail steel properties. These are the two main reasons why the Rayleigh wave polarization is used instead of the Rayleigh wave speed in this research.

Table 5.2 – Variations of TOE constants [GPa] and proportionality factors for an uncertainty of 20%

	υ_1	υ_2	υ_3	k^c	% diff	k^p	% diff
Min	-115.2	-304.8	-217.2	-2.69E-06	519.65%	1.34E-05	36.78%
Average	-96	-254	-181	-4.34E-07		9.76E-06	
Max	-76.8	-203.2	-144.8	1.82E-06	-519.64%	6.17E-06	-36.77%

5.2.3 Rayleigh Wave Polarization

The values of Rayleigh wave polarization are obtained by dividing the displacements in the x_1 direction by the displacements in the x_3 direction. These values can also be plotted against each other to visualize the shape of particle motion. Fig. 5.3 shows the change in the shape in particle motion between unstressed and stressed rail steel. Note that a compressive force of 10 GPa is used in this simulation for the purpose of enhanced illustration on how the shape of ellipse would change due to compressive force.
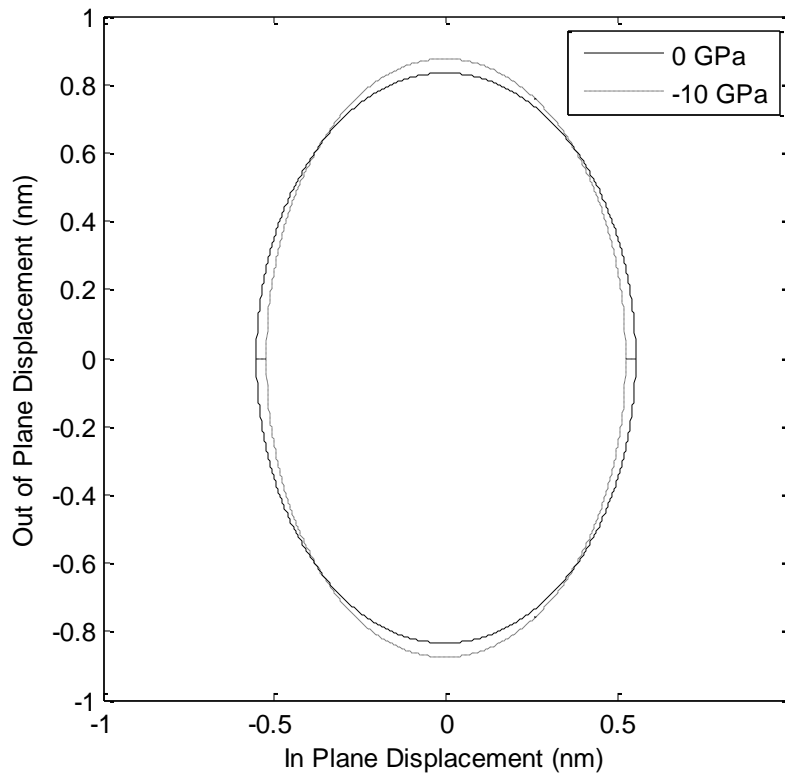
Fig. 5.3 – Trajectory plot of particle motion for unstressed and stressed rail

5.3 Frequency Range

Ideally, the Rayleigh wave theory is only valid for an elastic half-space. In this research, the Rayleigh wave is generated to propagate on the web of the rail. The web of the rail itself is a plate-like structure. Hence, a frequency range where the Rayleigh wave theory can be applied needs to be determined.

This propagation of Rayleigh wave itself is a superposition of the first antisymmetric and symmetric Lamb modes as explained by Viktorov (1966). Section 3.3 in this thesis explains about the Lamb waves modes in detail.

Masserey and Fromme (2008) investigated the propagation of Rayleigh waves in aluminum plates. The propagation of Rayleigh waves starts on the surface and gradually transfers to the other side of the plate, and then transfers back to the surface from which it started. The distance of that one whole cycle is called the beat length, calculated as

$$L = \frac{2\pi}{k_{a_0} - k_{s_0}} \quad ,$$

(5.6)

where k_{a_0} and k_{s_0} are the wave numbers of a_0 and s_0 modes respectively. Fig. 5.4 shows the wave number dispersion curve in a rail steel.
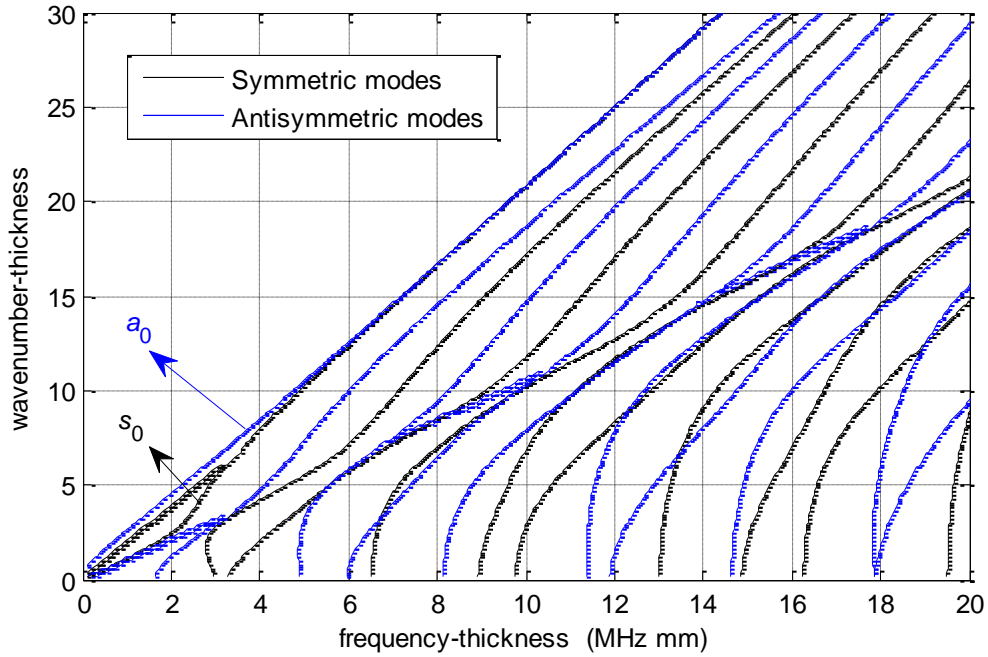
Fig. 5.4 – Rail steel dispersion curve

If the beat length approaches infinity, the amplitude of the Rayleigh wave is only decaying with distance. This could only be achieved when the denominator term

$(k_{a_0} - k_{s_0})$ approaches zero. In the dispersion curve chart (Fig. 5.4), increments in frequency-thickness results in decrements in the denominator term.
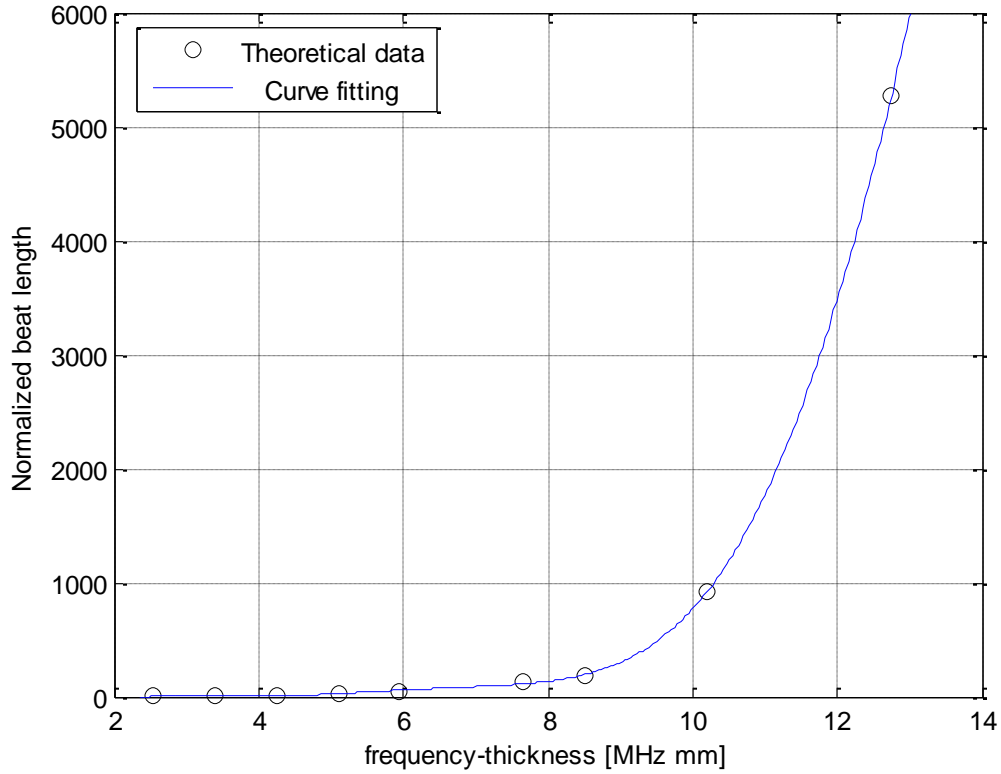
Fig. 5.5 – Normalized beat length L/h vs. frequency thickness fh with $h = 17$ mm

To determine the best frequency range, the normalized beat length L/h is plotted against frequency-thickness fh in Fig. 5.5. An assumption can be made that for a frequency-thickness greater than 10 MHz mm, the beat length approaches infinity, hence the amplitude of the Rayleigh wave is not dependent on distance. For a web thickness h of 17 mm (as used in the experiment), a frequency range of greater than 600 kHz is appropriate.

A test was conducted on rail steel with a length of 30 cm to find out how frequency range affects the attenuation of Rayleigh wave propagation. The test consists of finding the out-of-plane amplitude of the rail for 45 different locations starting at Location A (Fig. 5.6) and moving in increments of 4 mm further from the transducer to Location B. This test was done with excitation frequencies of 200 kHz and 1 MHz. Fig. 5.7 shows the plots of out-of-plane displacement amplitude vs. distance from transducer. With the excitation frequencies of 200 kHz, the amplitudes attenuated up to a certain distance, and then started to intensify again. While with the excitation frequencies of 1 MHz, the amplitudes of the Rayleigh wave decayed with distance and did not intensify for a long distance. This shows that the beat length effect does not show up on the rail steel with a frequency of 1 MHz. With these results, the future experiments are done with excitation frequency greater than 600 kHz.
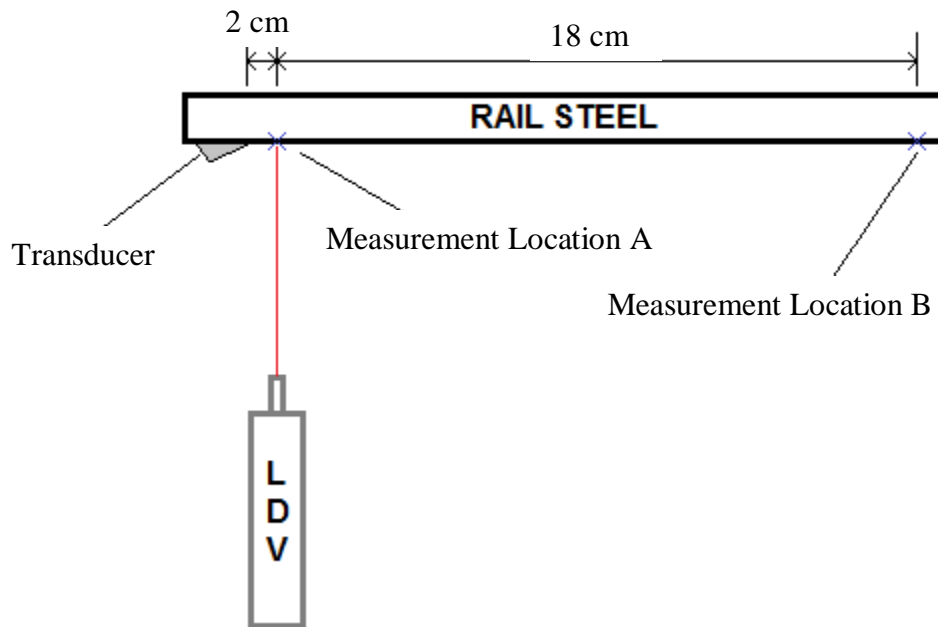
Fig. 5.6 – Experimental setup for finding frequency range
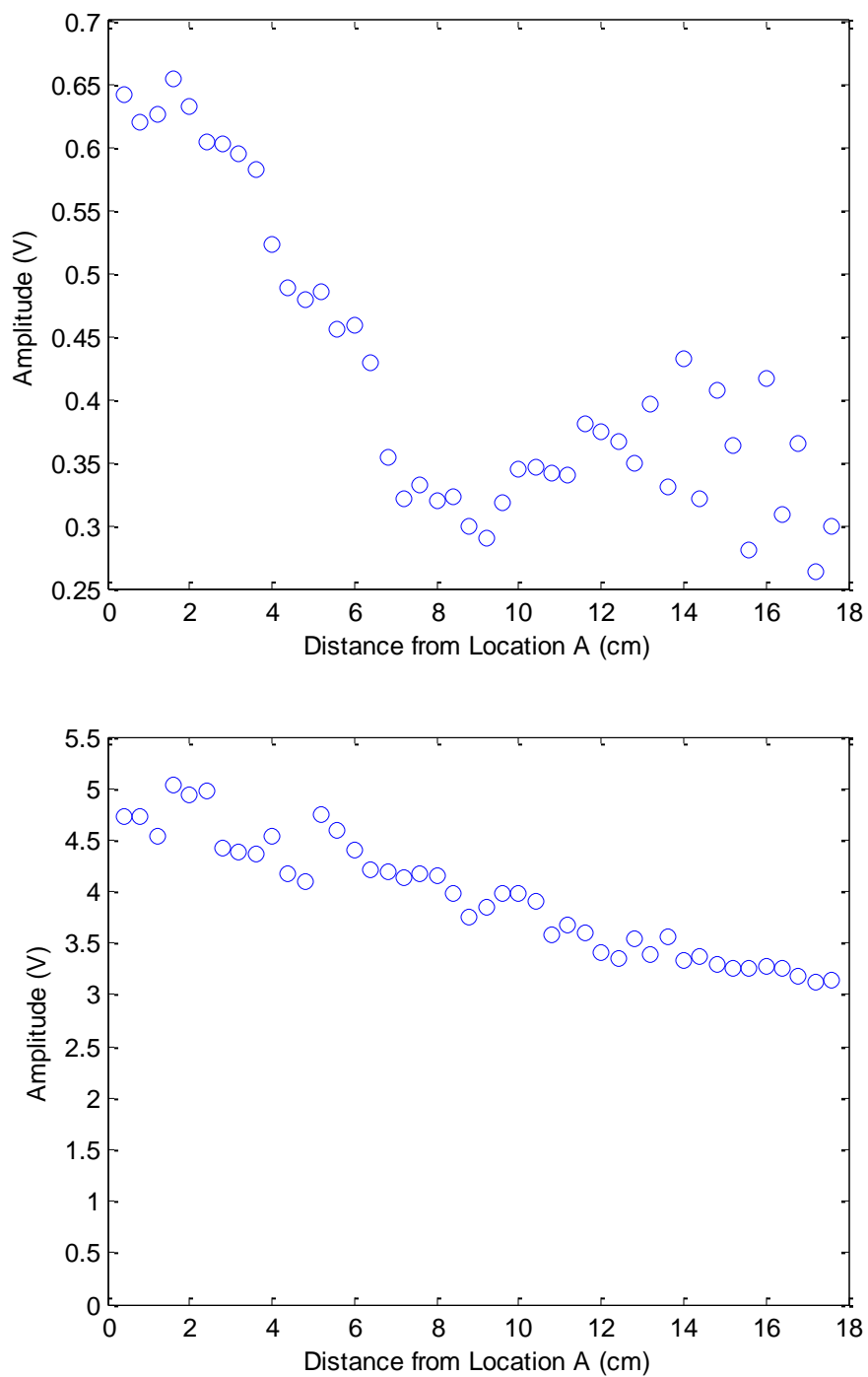
Fig. 5.7 – Out-of-plane displacement amplitude vs. distance from Location A with 200 kHz excitation (top) and 1 MHz excitation frequency (bottom)

CHAPTER VI

EXPERIMENTAL SETUP AND PROCEDURE

This first section of this chapter presents the experimental setup used in the investigation. The generation of Rayleigh wave using a wedge technique is discussed in the second section. The last section describes the experimental procedure to obtain the Rayleigh wave polarization.

6.1 Experimental Setup

The setup for this experiment can be seen in Fig. 6.1. A function generator is used to set up the signal's excitation frequency, amplitude, and number of burst cycle. The signal is then amplified using an RF amplifier. A wedge transducer generates a Rayleigh wave with the signal parameters set in the function generator. The particle velocity is then measured using an LDV. The signals are recorded with a digital storage oscilloscope (DSO) and transferred to a PC via RS232. The following sections discuss about the components involved in the experiment.

6.1.1 Function Generator and Amplifier

The experiment uses an Agilent 33250A function generator. The excitation frequencies used in this experiment are 800 kHz and 1 MHz with a burst signal of 10-cycle. The signal is amplified using a E8L RF Power Amplifier.
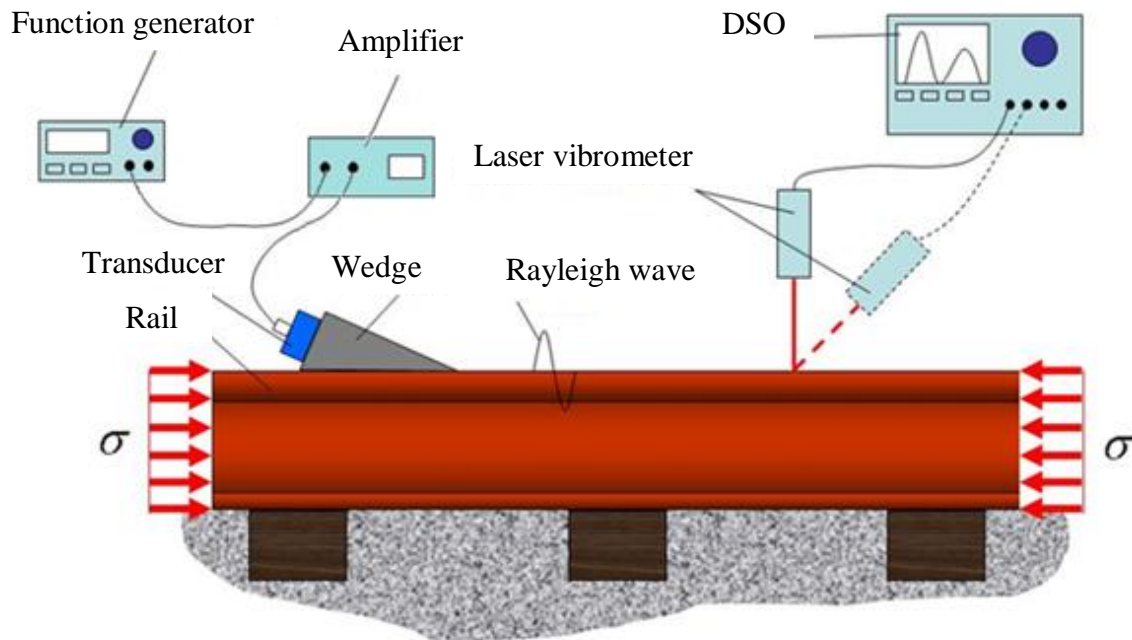
Fig. 6.1 – Experimental setup

6.1.2 Wedge Transducer

The transducer used in this experiment is a Centrascan series C401 from Panametrics with a center frequency of 1 MHz. This transducer is attached to an angle beam Panametrics wedge ABWX-2001. The transducer is set up at an incident angle of 65° from the plane perpendicular to the rail as specified in a later section to generate only Rayleigh waves to propagate in the rail.

6.1.3 Laser Doppler Vibrometer (LDV)

The Rayleigh wave detection is done using a Polytec single point vibrometer which consists of an OFV 505 standard sensor head and an OFV 5000 vibrometer controller. The basic concept of this vibrometer is to detect the frequency shift or phase

shift of the laser light that is reflected from a vibrating surface. This Doppler frequency (or phase) shift is then used to determine the surface velocity of the particles. A thorough review of laser vibrometer can be found in Hurlebaus, 2002 and Hurlebaus and Jacobs, 2006.

6.1.4 Data Acquisition

A Digital Storage Oscilloscope (DSO) Tektronix TDS 3034B is used to record the data captured by the LDV, and the signals are averaged 512 times by the oscilloscope. The data are transferred to a PC via RS232 using Wavestar software, and the data are analyzed using Matlab.

6.2 Generation of Rayleigh Waves Using the Wedge Technique

Wedge technique is a method that is used to generate only Rayleigh waves by setting a transducer mounted on the wedge at a specific incident angle of θ_w. Fig. 6.2 shows the picture of the transducer mounted on the wedge that is used in the experiments.

Fig. 6.2 – Wedge transducer

By looking at Fig. 6.3, the incident angle θ_w can be calculated as

$$\frac{\sin\theta_w}{\sin\theta_R} = \frac{c_l^{(1)}}{c_R^{(2)}} = \frac{\lambda_l^{(1)}}{\lambda_R^{(2)}} \ ,$$ (6.1)

where the superscript (1) and (2) denotes the first material (plexiglass wedge) and the second material (rail steel), respectively, and θ_R is the refracted angle with $\theta_R = 90^\circ$. This leads to

$$\sin\theta_w = \frac{c_l^{(1)}}{c_R^{(2)}} \ .$$ (6.2)

Eq. (6.2) proves that this technique only works if the Rayleigh wave speed of the specimen, $c_R^{(2)}$, is greater than the longitudinal wave speed of the plexiglass, $c_l^{(1)}$.
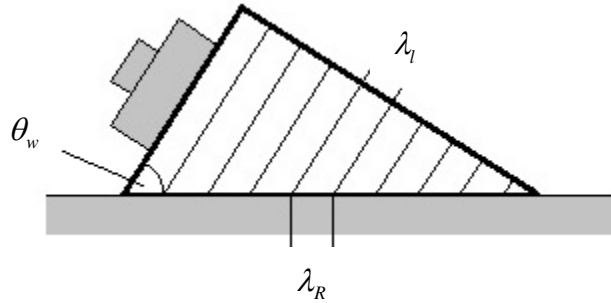
Fig. 6.3 – Schematic figure of wedge transducer (*Junge, 2003*)

The typical Rayleigh wave speed for rail steel is 3000 m/s, and the longitudinal wave speed of the plexiglass wedge is 2720 m/s. By using Eq. (6.2), the incident angle θ_w needed to generate a Rayleigh wave on rail steel is 65°.

Theoretically, when the incident angle θ_w is used on the transducer to generate a Rayleigh wave, shear waves and longitudinal waves will not be transmitted by the transducer. This perfect mode conversion from longitudinal wave to Rayleigh wave is one advantage of using a wedge technique. This is true because Rayleigh wave speed is always smaller than the shear and longitudinal waves speed. By utilizing the incident angle in Eq. (6.2), the angle of the transmitted shear and longitudinal waves are

$$\sin\theta_l = \sin\theta_w \cdot \frac{c_l^{(2)}}{c_l^{(1)}} = \frac{c_l^{(2)}}{c_R^{(2)}} > 1 \ , \tag{6.3}$$

$$\sin\theta_s = \sin\theta_w \cdot \frac{c_s^{(2)}}{c_l^{(1)}} = \frac{c_s^{(2)}}{c_R^{(2)}} > 1 \ . \tag{6.4}$$

Eq. (6.3) and Eq. (6.4) prove that both shear and longitudinal wave speed are not transmitted since the solutions for both angles do not exist. Another advantage of using the wedge technique is that this method is valid for all frequency ranges without changing the incident angle. The perfect mode conversion also applies for its waveforms. For example, a longitudinal wave with a sinusoidal waveform will stay as a sinusoidal waveform when it is mode converted to a Rayleigh wave.

6.3 Experimental Procedures

To obtain the in-plane and out-of-plane components, measurements from two different angles are necessary. Fig. 6.4 shows the geometrical variables for the in-plane and out-of-plane components calculation
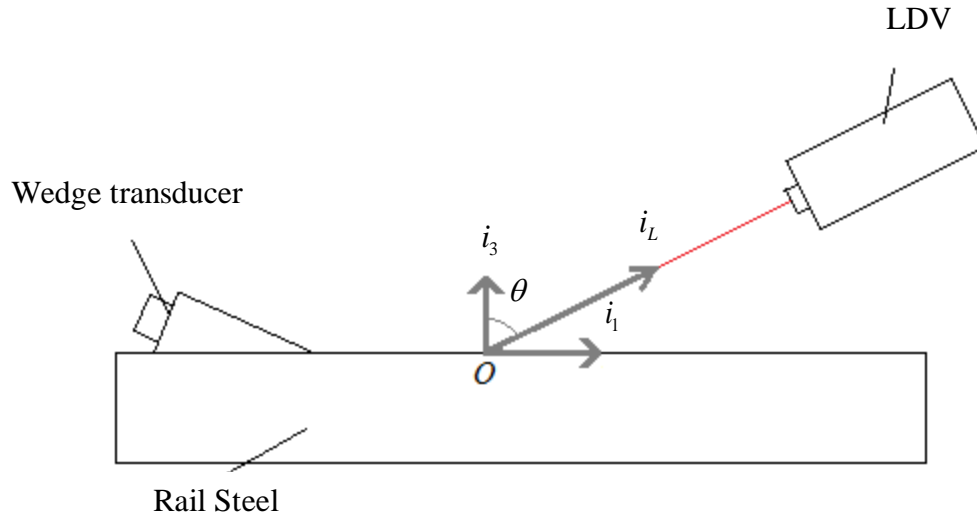
Fig 6.4 – Geometrical variables for in-plane and out-of-plane components

Let the velocity at point O be

$$v = u_1 i_1 + u_3 i_3 \ , \tag{6.5}$$

where u_1 and u_3 represent the in-plane and out-of-plane velocity components at point O, respectively. The velocity component measured by the LDV, u_L, can be expressed by

$$u_L = v \cdot i_L \ , \tag{6.6}$$

where

$$i_L = \sin\theta i_1 + \cos\theta i_3 \ , \tag{6.7}$$

which yields

$$u_L = u_1 \sin\theta + u_3 \cos\theta \ . \tag{6.8}$$

To determine u_1 and u_3, two measurements from two different angles, θ_a and θ_b, are needed to obtain two equations of Eq. (6.8), which leads to

$$\left\{ \begin{array}{c} u_L^{(a)} \\ u_L^{(b)} \end{array} \right\} = \left[\begin{array}{cc} \sin\theta_a & \cos\theta_a \\ \sin\theta_b & \cos\theta_b \end{array} \right] \left\{ \begin{array}{c} u_1 \\ u_3 \end{array} \right\} . \tag{6.9}$$

The solution of the in-plane and out-of-plane components yield to be

$$\left\{ \begin{array}{c} u_1 \\ u_3 \end{array} \right\} = \frac{1}{\sin(\theta_b - \theta_a)} \left[\begin{array}{cc} -\cos\theta_b & \cos\theta_a \\ \sin\theta_b & -\sin\theta_a \end{array} \right] \left\{ \begin{array}{c} u_L^{(a)} \\ u_L^{(b)} \end{array} \right\} , \tag{6.10}$$

where u_1 and u_3 are the in-plane and out-of-plane velocity components, respectively, θ_a and θ_b are the angles measured from the axis perpendicular to the rail, and $u_L^{(a)}$ and $u_L^{(b)}$ are the velocity components measured under the angle of θ_a and θ_b, respectively.

Figure 6.5 shows the schematic of experimental setup used to take measurements from two different angles. The first measurement is taken by setting the LDV perpendicular to the rail ($\theta_a = 0^\circ$) to measure the out-of-plane velocity. The second measurement is done by placing two mirrors in the path of the laser with the intention of getting the measurement θ_b from the out-of-plane axis. Mirror 1 is fixed on the optical table, while Mirror 2 is fixed on a translation stage. Using the translation stage helps in getting reproducible results since Mirror 2 can be placed to a desired location with the accuracy of 0.01 mm.
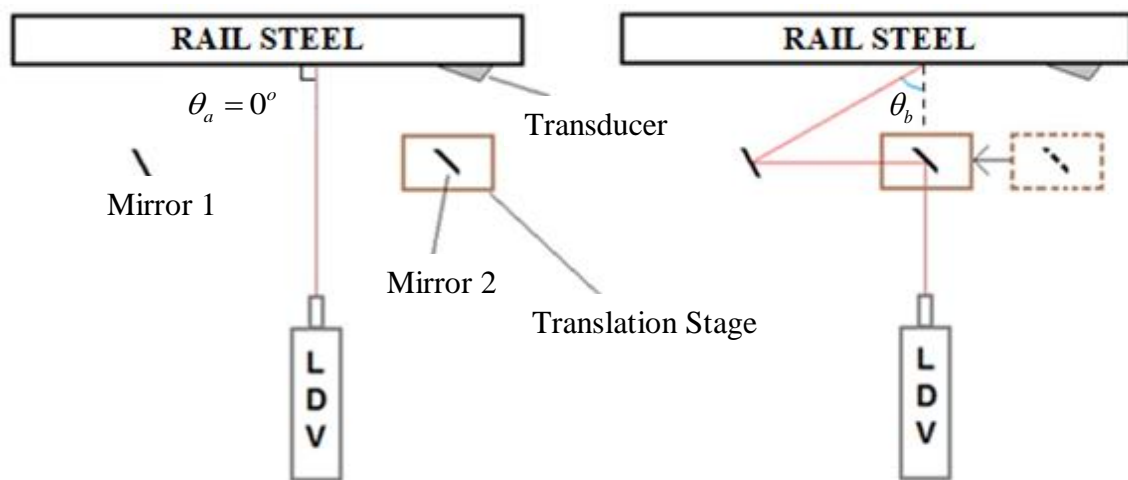
Fig 6.5 – Schematic of experimental setup

CHAPTER VII

EXPERIMENTAL RESULTS

The experimental results are explained in this section. Also, further investigations on the effect of focusing the light from LDV and the effect of surface preparation on the LDV carrier signal are discussed. Finally, the results of the experiment using a reflective tape on the rail surface will be described.

7.1. Experimental Results

The use of signal processing is very crucial for getting the right orientation of Rayleigh wave polarization experimentally. The experimental results of the Rayleigh wave polarization with and without using the signal processing technique are compared and explained in this section. The experimental results on unstressed and stressed rail are presented and compared with the theoretical data.

7.1.1 Experimental Results Before and After Signal Processing

Measurements from two different angles are necessary to determine the in-plane and out-of-plane particle displacements. Once both of these particle displacements are obtained, they are plotted against each other to obtain the Rayleigh wave polarization.

An experiment was done to obtain the polarization of Rayleigh wave with and without using signal processing. The excitation frequency used was 800 kHz, and the

sampling frequency was set to 250 MHz. The angles used in this experiment were $\theta_a =$ 0° and $\theta_b = 40^o$ (see Fig 6.4).
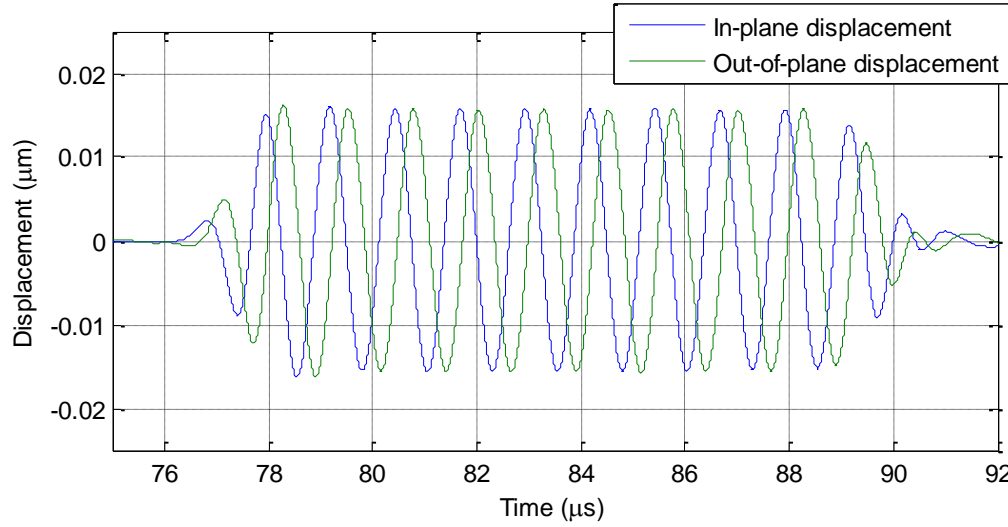
Fig. 7.1 – In-plane and out-of-plane displacement components in time domain without using signal processing
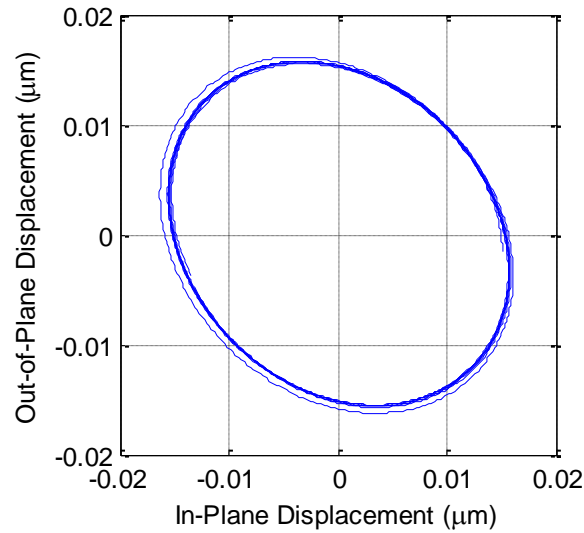
Fig. 7.2 – Rayleigh wave polarization without using signal processing

Fig. 7.1 and Fig. 7.2 show the experimental results without using signal processing. The result showed that the Rayleigh wave polarization was not in the right orientation. This occurred because the phase shift between the in-plane and out-of-plane particle displacements was not exactly 90° or $\pi/2$.

To obtain a phase shift of exactly $\pi/2$ between the in-plane and out-of-plane particle displacements, a technique is needed in the signal processing. This is used to find the phase shift between the actual time domain signal and the expected time domain signal of the out of plane particle displacement. Once the phase shift is determined, the raw out-of-plane particle velocity has to be shifted accordingly. Fig. 7.3 shows the plot of raw out-of-plane particle velocity before and after using signal processing. In this experiment, the phase shift between them was only 0.05 µs or 14°.
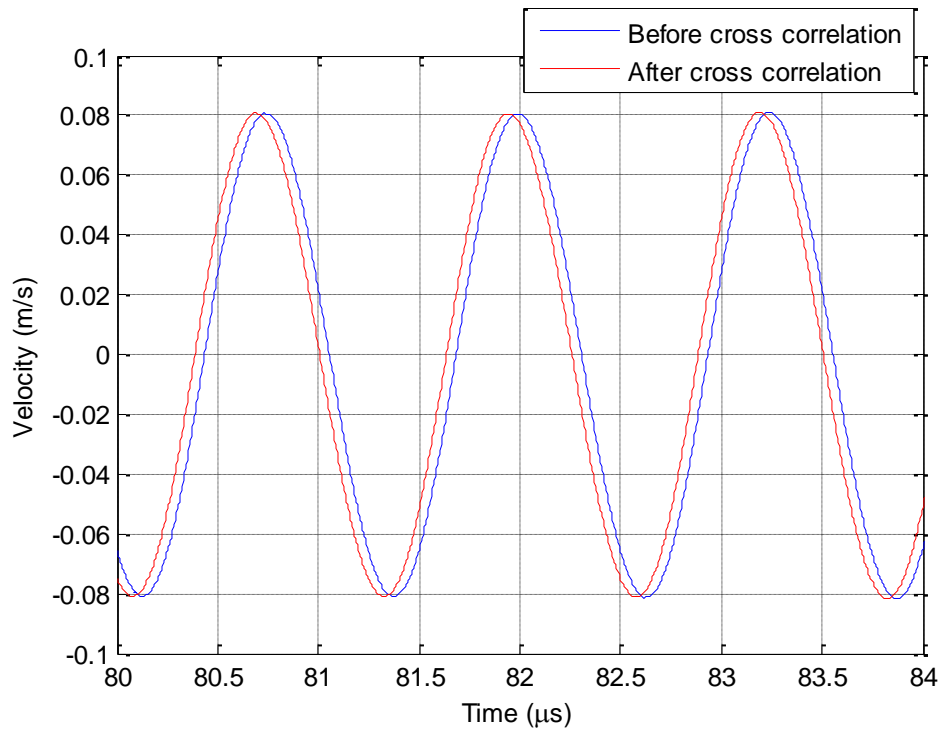
Fig. 7.3 – Out-of-plane velocity before and after cross correlation
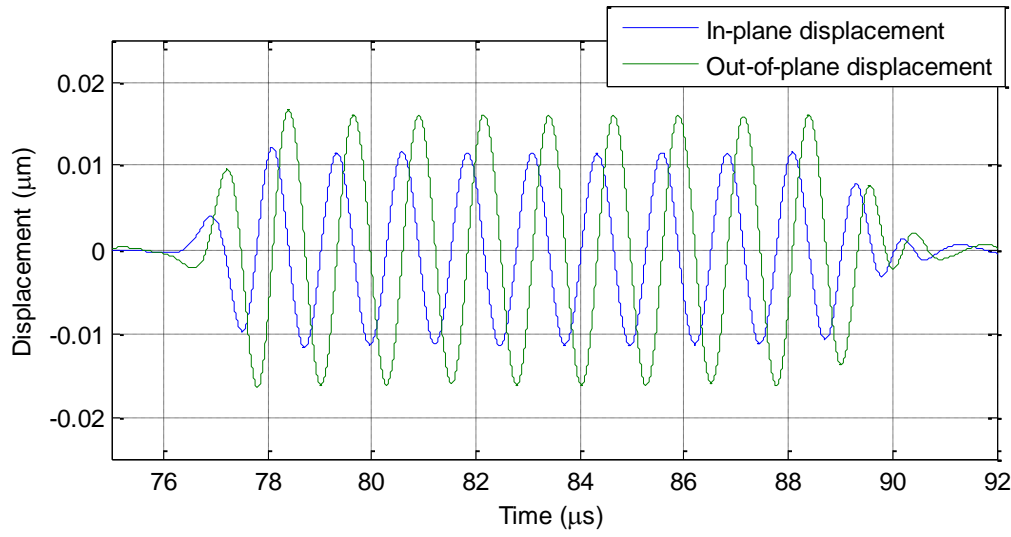
**Fig. 7.4** – In-plane and out-of-plane displacement components in time domain using signal processing
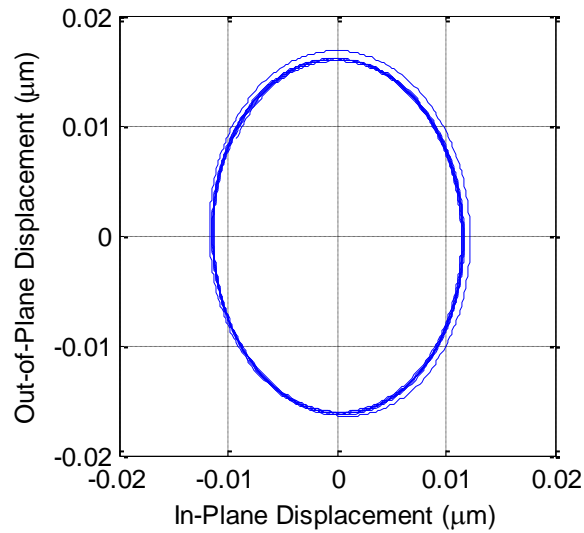
Fig. 7.5 – Rayleigh wave polarization using signal processing

Fig. 7.4 and Fig. 7.5 show the experimental results using signal processing. The signal processing technique shows that the phase shift of 0.05 µs or 14° between the out-of-plane particle velocity components changes the result significantly. Without this

technique, it is very difficult to obtain the Rayleigh wave polarization with the right orientation. One way to do this is to take the measurements from two different angles exactly on the same spot. With Rayleigh wave speed of 3000 m/s propagating on the rail, the phase shift of 0.05 μs means that the location spot of the measurements from two different angles was off by 0.15 mm. Thus, this technique becomes a very important part in the signal processing.

7.1.2 Unstressed Rail Steel

In this experiment, an excitation frequency of 800 kHz was used, and the sampling frequency was set to 250 MHz. The experiment was done using the angles of $\theta_a = 0^o$ and $\theta_b = 40^o$. The time domain signal of raw data can be seen in Fig. 7.6. As expected, only Rayleigh wave was identified in the plot due to the wedge technique.

After analyzing the raw data, the in-plane and out-of-plane displacement components were obtained, and the plot can be seen in Fig. 7.7. The in-plane and out-of-plane displacement components are plotted against each other, and the value of Rayleigh wave polarization can be calculated. The polarization plot is shown in Fig. 7.8. As expected, the shape of Rayleigh wave polarization is in a form of an ellipse.
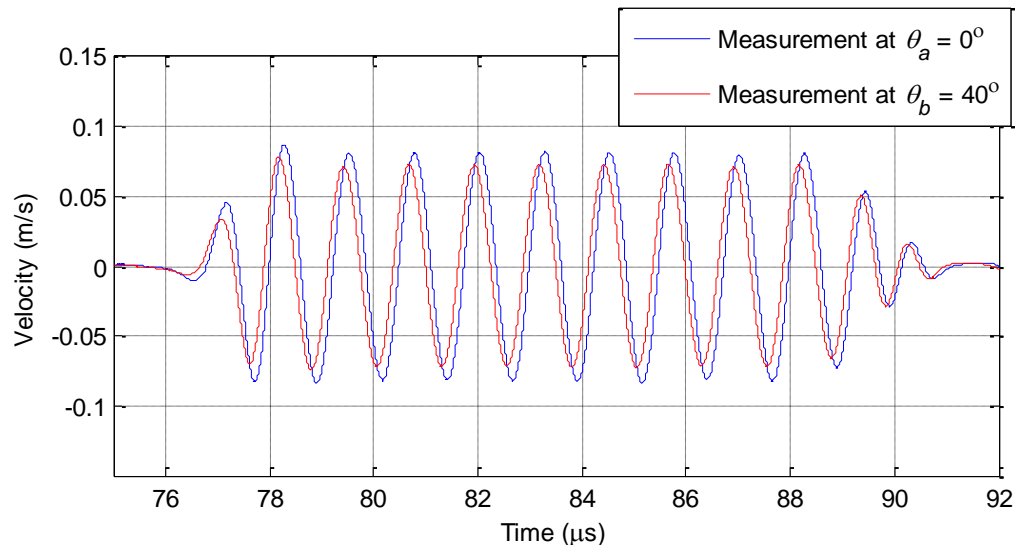
Fig. 7.6 – Raw velocity components in time domain
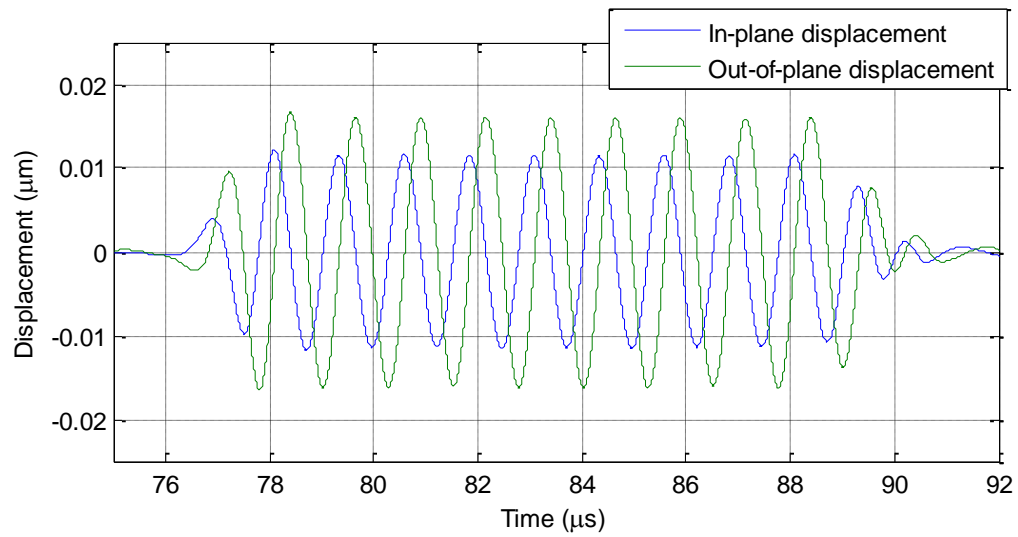
Fig. 7.7 – In-plane and out-of-plane displacements in time domain
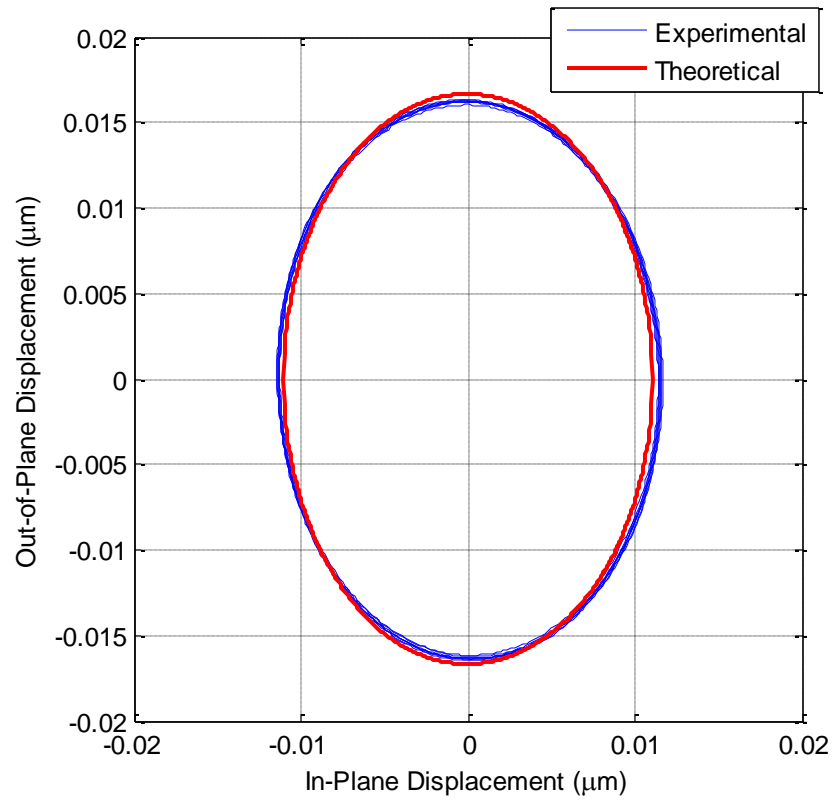
Fig. 7.8 – Polarization of Rayleigh wave

This experiment was performed ten times. The graphs in Fig. 7.6, Fig. 7.7, and Fig. 7.8 show the results from the first experiment. The values of the results are presented in Table 7.1. The difference between the theoretical Rayleigh wave polarization and the mean experimental polarization is 0.0611. This yields a percent error of 9.21%.

Table 7.1 – Polarization value for unstressed rail

Theoretical polarization	Mean experimental polarization	Standard deviation	Coefficient of variation
0.6631	0.7242	0.0134	1.86%

The length of the rail used in this experiment might be a factor in the difference between the experimental and theoretical results. The specimen used in this experiment was a 1-foot rail steel. End effects could appear with this size of rail, which would disturb the Rayleigh wave signal. The signal quality of the LDV might also be the factor that causes this difference. Different measurement locations give different signal quality. To improve this quality, investigation on the surface preparation is needed. The investigation on the effect of surface preparation on the signal quality is described in Section 7.3.

7.1.3 Stressed Rail

The test was done at Transportation Technology Center, Inc. (TTCI) facilities in Pueblo, CO. The condition of the rail was used with a length of 15 ft**.** Fig. 7.9 shows the experimental setup at TTCI.

This experiment used an excitation frequency of 800 kHz and sampling frequency of 250 MHz. The angles used in this experiment were $\theta_a = 0^o$ and $\theta_b = 60^o$. Fig 7.10 shows the plot of normalized polarization of Rayleigh wave vs. normalized loads. As expected, the polarization value increases with increasing tension load.

Fig. 7.9 – Experimental setup at Pueblo, CO.
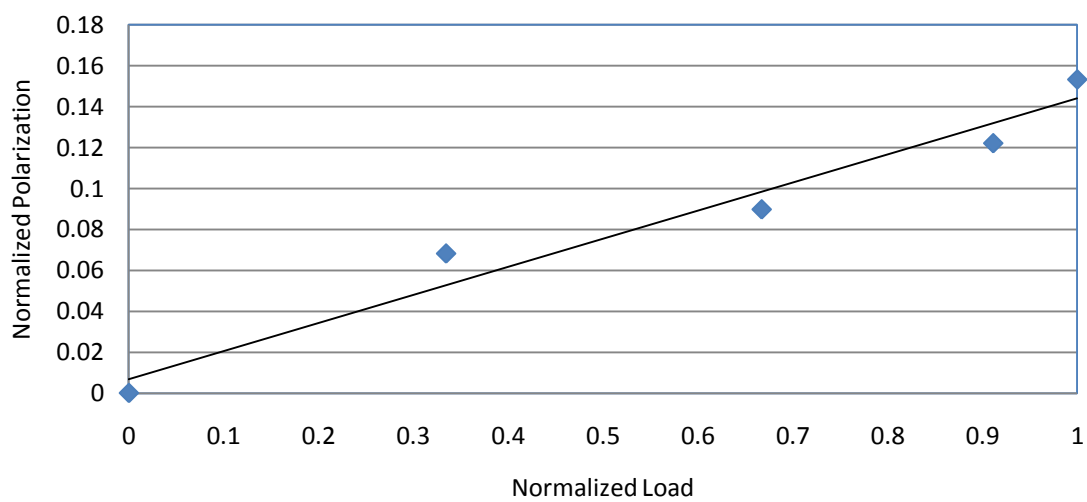
Fig. 7.10 – Normalized polarization vs. normalized load

7.2 The Effect of Focusing

When using LDV to measure the particle velocity components, the incident light is focused on a very small spot on the specimen for two purposes. The first purpose is that the instantaneous particle velocity within that spot can be assumed to be the same when the incident light spot is very small (Kil et al. 1998). The second purpose is to get the best carrier signal from the LDV sensor head to increase SNR.

There are two ways to focus the laser light on the specimen. These are manual focus and auto focus. The results from obtained these focusing modes are discussed. Although focusing the laser light gives the best carrier signal, there is a situation where unfocused laser light gives better carrier signal than the focused light. The results obtained from focused and unfocused light are presented in this section.

7.2.1 Manual Focus vs. Auto Focus

An experiment was conducted to compare the results obtained from manual focus and auto focus. The excitation frequency used in this experiment was 1 MHz with a sampling frequency of 250 MHz, and a 10-cycle burst was set. For each mode, five measurements of the particle velocity were taken using LDV from 40° from the axis perpendicular from the rail, and one measurement of the out-of-plane particle velocity was taken for the purpose of calculating the Rayleigh wave polarization values. The phase shift, the amplitude variation, and the polarization variation between each measurement were evaluated through these data with respect to measurement No. 1. Table 7.2 and Table 7.3 show these results. Since this experiment used a 10-cycle burst,

the Rayleigh wave consisted of 10 sinusoidal wave cycles, and the mean amplitude of the ten maxima and ten minima were calculated instead of just using the maximum value for a better result.

Table 7.2 - Phase shift and amplitude difference under manual focusing

Comparison between measurement No.	Phase shift (us)	Mean amplitude difference	Difference in polarization value
1 & 2	0	0.09%	1.07%
1 & 3	0	0.07%	1.64%
1 & 4	0	0.24%	0.23%
1 & 5	0.004	0.35%	0.69%

Table 7.3 - Phase shift and amplitude difference under auto focusing

Comparison between experiment No.	Phase shift (us)	Mean amplitude difference	Difference in polarization value
1 & 2	0.0035	0.85%	0.54%
1 & 3	0.004	1.27%	2.67%
1 & 4	0.0065	1.70%	5.05%
1 & 5	0.011	2.12%	4.24%

As can be seen in both Table 7.2 and Table 7.3, the auto focus mode yields more variance in its phase shift and mean amplitude difference which leads to more inconsistency in the polarization values. In manual focusing, the phase shift happened in the fifth measurement, while in auto focusing, the phase shift already happened in the second measurement. The mean amplitude difference in manual focusing reached up to 0.35%, while the mean amplitude difference in auto focusing reached up to more than 2%. The difference in polarization value yielded less than 2% in manual focusing, while the polarization value difference in auto focusing yielded up to 5%. With these data, we

can conclude than the manual focusing is more consistent in taking multiple measurements than the auto focus mode.

7.2.2 Focused vs. Unfocused

There was a situation, although uncommon, where focusing the incident light to the smallest spot did not yield the best carrier signal. In that case, the incident light had to be unfocused on a slightly larger spot to obtain the best carrier signal. That means the LDV has to operate under the condition of best carrier signal but unfocused, or focused but not under the best carrier signal. For the purposes of comparison, the condition of focused light but not under the best carrier signal is named Case A, and the condition of unfocused light but under the best signal is named Case B.

An experiment was done to investigate the effect of Case A and Case B. Using the same experimental setup as the experiment of comparing manual focus and auto focus, five sets of particle velocity measurement were taken using LDV from 40° from the axis perpendicular to the rail, and one set of measurement of the out-of-plane particle velocity was taken for the purpose of calculating the Rayleigh wave polarization. Each set consisted of one measurement of Case A and one measurement of Case B.
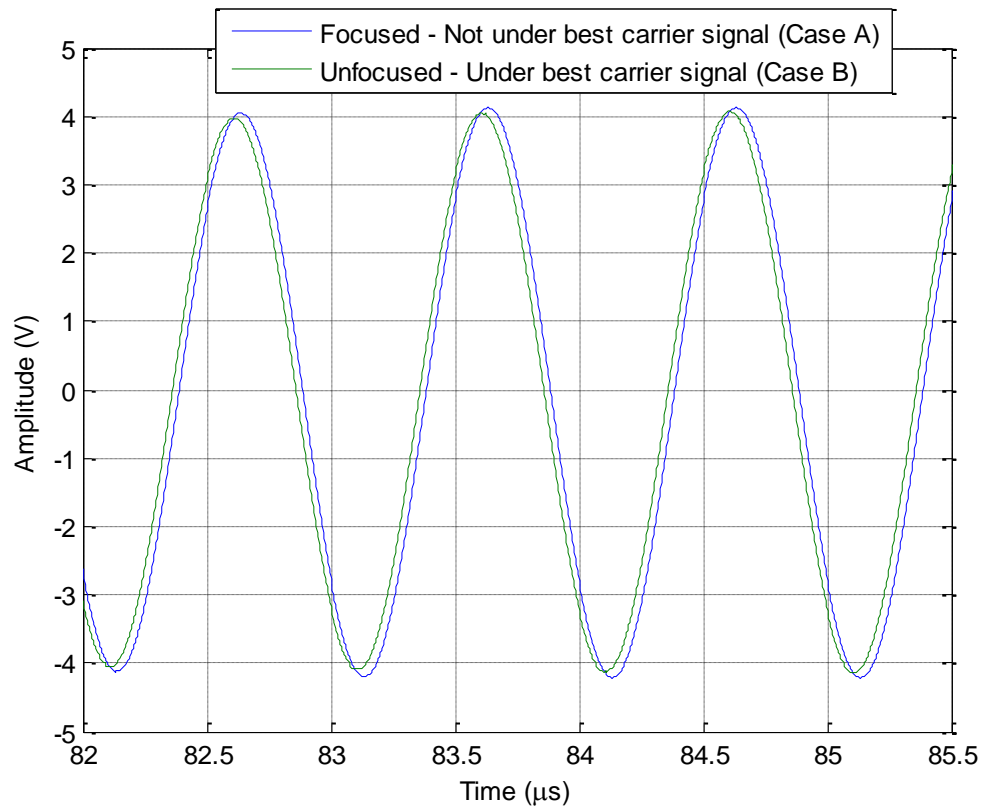
Fig. 7.11 – Raw data of component under 40° from the plane normal to the rail for Case A (blue) and Case B (green)

Fig. 7.11 shows the time domain signal of the velocity component under 40° from the plane normal to the rail. The plot shows that there is a phase shift and there is a change in amplitude. The phase shift, mean amplitude difference, and the polarization difference between Case A and Case B of each set are shown in Table 7.4. The mean amplitude difference between Case A and Case B is the main cause of the polarization difference. Table 7.4 shows that the values of polarization difference between both cases of all sets range from 4% to 7%. In Table 7.2, where focusing on the smallest light spot gives the best carrier signal, the polarization difference between the repeating measurements is about 1%. This shows a significant difference between them.

Theoretically, the polarization values of the unstressed rail and the rail under a compression load of 25 tons are 0.66307 and 0.66287, respectively. This yields a percent difference of 0.03%. With these data, the values of polarization difference shown in Table 7.4 are very large compared to the values of polarization difference shown in Table 7.2. In conclusion, if a situation of Case A or Case B occurs, the measurement spot has to be changed to another location where the best carrier signal can be achieved when the laser is most focused.

Table 7.4 - Phase shift, mean amplitude difference, and polarization
difference between Case A and Case B

Experiment	Phase shift (us)	Mean Amplitude difference (V)	Polarization difference
Set 1	0.025	1.76%	6.58%
Set 2	0.03	1.59%	5.00%
Set 3	0.03	0.93%	4.45%
Set 4	0.03	1.31%	3.98%
Set 5	0.03	1.48%	7.08%

7.3. The Effect of Surface Preparation on the Quality of Carrier Signal

The quality of LDV carrier signals depends on the amount of light reflected back to the laser head. To achieve a good quality signal from the rail steel, its surface needs to be treated. An experiment was conducted on steel plates to determine what kind of preparations are needed in order to have a surface that will give the best quality of LDV carrier signal.

Each steel plate received one kind of surface treatment. A laser light from LDV was focused to each of these plates starting at an angle of 0° (out-of-plane) to an angle of 80° from the axis perpendicular to the surface. For each angle, 10 measurements were taken on 10 different spots. These measurement spots were marked, where each mark was located 1 mm away from the previous mark.

There were several kinds of surface preparations applied on the steel plates. The steel plates were grinded, sanded, polished, sand blasted, sprayed with different kind of reflective spray, glued with reflective tape, and coated with Axon Reflective coating. In all the steel plates that were sanded, they were all grinded first. The steel plates were finished with grit 60, 100, 120, 150, 240, 500. The reflective sprays used in the experiment were Rustoleum Reflective Finish, Zyglo Developer, Sphere Brite Night Vision, and Flat Protective Enamel.

Table 7.5 shows the quality of the carrier signal for all steel plates with different surface preparations. Note that the quality of the signal is represented with bars, where a full signal gets 20 bars. The results show that the best surface preparation is to apply a reflective tape. The quality of the signal using a reflective tape is perfect up to an angle of 50° from the out-of-plane axis. It also has the lowest coefficient of variation (CoV) values compared to the other surface preparations.

Table 7.5 – Quality of LDV carrier signals under different surface preparations (unit is in bars). The angles shown in this table are measured from the plane normal to the rail

Surface treatment		Quality of the signal under angle of								
		0º	10º	20º	30º	40º	50º	60º	70º	80º
Untreated	Average	1.8	3.9	4.1	2.4	2.5	0.3	0.3	0.1	0.0
	Std Dev	1.8	2.7	1.4	1.5	2.0	0.7	0.7	0.3	0.0
	CoV	97%	69%	33%	63%	81%	225%	225%	316%	0%
Grinded	Average	19.6	5.5	0.2	0.8	0.1	0.0	0.0	0.0	0.0
	Std Dev	0.8	2.4	0.4	2.5	0.3	0.0	0.0	0.0	0.0
	CoV	4%	44%	211%	316%	316%	0%	0%	0%	0%
Sand paper Grit 60	Average	12.8	7.1	3.0	2.0	0.5	0.0	0.0	0.0	0.0
	Std Dev	2.7	2.5	1.9	2.9	0.8	0.0	0.0	0.0	0.0
	CoV	21%	35%	65%	143%	170%	0%	0%	0%	0%
Sand paper Grit 100	Average	13.6	7.1	4.7	1.2	0.9	0.1	0.0	0.1	0.0
	Std Dev	3.7	1.5	2.2	1.3	0.6	0.3	0.0	0.3	0.0
	CoV	27%	21%	47%	110%	63%	316%	0%	316%	0%
Sand paper Grit 120	Average	17.2	6.0	3.7	0.6	0.1	0.0	0.0	0.0	0.0
	Std Dev	3.1	3.0	3.1	1.1	0.3	0.0	0.0	0.0	0.0
	CoV	18%	50%	85%	179%	316%	0%	0%	0%	0%
Sand paper Grit 150	Average	15.5	6.4	2.7	1.6	0.2	0.0	0.0	0.0	0.0
	Std Dev	2.6	1.6	1.8	1.6	0.4	0.0	0.0	0.0	0.0
	CoV	17%	26%	65%	99%	211%	0%	0%	0%	0%
Sand paper Grit 240	Average	14.9	6.9	4.0	3.3	0.8	0.1	0.0	0.0	0.0
	Std Dev	3.4	2.6	2.0	2.5	1.5	0.3	0.0	0.0	0.0
	CoV	23%	38%	50%	76%	184%	316%	0%	0%	0%
Sand paper Grit 500	Average	18.3	5.0	3.1	1.3	0.6	0.2	0.0	0.0	0.0
	Std Dev	2.5	1.6	1.6	1.4	0.7	0.6	0.0	0.0	0.0
	CoV	14%	31%	51%	109%	117%	316%	0%	0%	0%
Polished	Average	20.0	0.9	0.0	0.0	0.0	0.0	0.0	0.0	0.0
	Std Dev	0.0	1.2	0.0	0.0	0.0	0.0	0.0	0.0	0.0
	CoV	0%	133%	0%	0%	0%	0%	0%	0%	0%
Sand Blasted	Average	6.8	7.8	7.6	6.7	6.1	5.4	4.5	4.1	3.4
	Std Dev	1.4	2.0	2.1	1.3	2.2	2.1	2.0	1.2	2.0
	CoV	21%	26%	27%	20%	37%	38%	45%	29%	58%
Developer	Average	5.9	6.3	8.3	7.4	7.1	5.8	3.6	5.0	0.0
	Std Dev	1.6	1.3	1.9	2.4	2.2	1.8	2.5	1.7	0.0
	CoV	27%	21%	23%	32%	31%	31%	68%	34%	0%

Table 7.5 - continued

Surface treatment		Quality of the signal under angle of								
		0°	10°	20°	30°	40°	50°	60°	70°	80°
Reflective Finish	Average	19.7	5.5	1.5	1.1	0.2	1.1	0.0	0.0	0.0
	Std Dev	0.9	2.5	1.9	2.8	0.6	3.5	0.0	0.0	0.0
	CoV	5%	46%	127%	259%	316%	316%	0%	0%	0%
Reflective Tape	Average	20.0	20.0	20.0	20.0	20.0	20.0	16.9	11.0	0.8
	Std Dev	0.0	0.0	0.0	0.0	0.0	0.0	1.5	3.3	1.1
	CoV	0%	0%	0%	0%	0%	0%	9%	30%	142%
Sphere Brite	Average	11.6	12.5	16.1	13.9	11.8	11.9	9.1	8.2	7.8
	Std Dev	5.0	4.3	2.7	4.1	3.5	6.3	4.7	4.0	4.7
	CoV	43%	34%	17%	30%	30%	53%	52%	49%	60%
Flat Protective Enamel	Average	3.6	2.7	3.0	1.5	2.6	3.7	3.7	2.8	2.7
	Std Dev	3.7	2.6	3.3	1.9	2.8	2.1	2.5	2.7	2.4
	CoV	104%	96%	111%	127%	108%	56%	69%	98%	87%
Axon Reflective Coating	Average	7.4	3.6	2.7	2.0	0.9	1.4	1.5	2.1	1.2
	Std Dev	4.6	3.2	2.6	3.1	1.7	1.8	3.6	3.7	2.0
	CoV	62%	90%	96%	153%	185%	127%	238%	175%	166%

7.4 Conclusion

The experimental results show that signal processing is very crucial in getting the right orientation of Rayleigh wave polarization. The result on the unstressed rail shows a good agreement with the analytical result. However, to be able to take a measurement on the rail surface, surface preparation is needed.

In the investigation to determine the effect of focusing the light on the specimen, manual focus mode proves to be more stable in obtaining the results than the auto-focus mode. Also, in the situation where focusing on the smallest spot does not give the best carrier signal, the location needs to be changed so that focusing on the smallest spot gives the best carrier signal.

The experiment of determining the effect of surface preparation on the quality of LDV carrier signal that was performed on steel plates shows that reflective tape is the best surface preparation in getting the best carrier signal.

CHAPTER VIII

CONCLUSIONS AND FUTURE WORK

This research investigates a method of determining the stress in rails by using the polarization of Rayleigh waves generated by a wedge transducer. The relationship between the polarization of Rayleigh waves and the state of stress can be seen in the analytical model. The numerical simulation shows that the change of polarization of Rayleigh wave on residual stress is one order of magnitude higher than the change of Rayleigh wave speed; thus, Rayleigh wave polarization in more sensitive to applied stress. In addition, sensitivity analysis shows that the polarization of Rayleigh wave is more robust against uncertainties in material properties. These results conclude that Rayleigh wave polarization is more sensitive and more robust than the Rayleigh wave speed. These are the two main reasons why Rayleigh wave polarization is used instead of Rayleigh wave speed in this research.

This proposed method is a non-destructive measurement technique that is not labor intensive. The measurement of polarization is a point wise measurement, which means that the applied stress on rail can be determined just by measuring the polarization from a single point. This method is also a reference-free measurement. No information about the propagation distance is needed to do the measurement. Also, this technique does not have the disadvantage of being integral. The influence of material properties is not accumulated along the propagation path of the wave. The combination

of these benefits is the advantage of this method that other methods do not have. The experimental results of Rayleigh wave polarization for unstressed rail shows a good agreement with the analytical result.

The following recommendations are suggested for future work:

1.   Increase the laser power of the LDV

Maintaining sufficient laser energy is very important to avoid the loss of carrier signal of the LDV. By increasing the power of the LDV, the laser energy will increase, and the loss of carrier signal will be minimized.

2.   Replace the wedge transducer with a non-contact laser generation

The use of laser generation makes this technique to be a non-contact measurement. With the non-contact measurement method, this system can be applied on a running train.

REFERENCES

Bray, D. E. (2002). "Ultrasonic Stress Measurement in Pressure Vessels, Piping, and Welds." *Journal of Pressure Vessel Technology,* 124 (3), 326-335.

Bray, D. E., and Leon, T. (1985). "Zero-Force Travel-Time Parameters for Ultrasonic Head-Waves in Railroad Rail." *Material Evaluation,* 43, 854-863.

Crecraft, D. I. (1962). "Ultrasonic Wave Velocities in Stresses Nickel Steel." *Nature*, 195(4847), 1193.

Crecraft, D. I. (1967). "The Measurement of Applied and Residual Stresses in Metals for Measurement of Contained Stress in Railroad Rail." *Journal and Sound Vibration*, 5(1), 173-192.

Damljanovic, V. and Weaver, R.L. (2005). "Laser Vibrometer Technique for Measurement of Contained Stress in Railroad Rail." *Journal of Sound and Vibration*, 282, 341-366.

Duquennoy, M. and Ouaftough, M. and Ourak, M. (1999). "Ultrasonic Evaluation of Stresses in Orthotropic Materials Using Rayleigh Waves." *NDT&E International*. 32(4), 189-199.

Egle, D. M. and Bray, E. D. (1976). "Measurement of Acousto-elastic and Third-order Elastic Constants for Rail Steel." *Journal of the Accoustical Society of America*, 60, 741-744.

Egle, D. M. and Bray, D. E. (1979). "Application of the Acousto-Elastic Effect to Rail Stress Measurements." *Material Evaluation,* 37, 41-55.

Gokhale, S. (2007). "Determination of Applied Stresses in Rails Using the Acoustoelastic Effect of Ultrasonic Waves." M.S. Thesis, Texas A&M University, College Station, TX.

Graff, K.F. (1991). *Wave Motion in Elastic Solids*. Dover Publications Inc., New York.

Hayes, A.P. (2008). "MAPS-SFT, a New Tool in the Infrastructure Manager's Toolbox." MAPS Technology Ltd, UK.

Hirao, M., and Fukuoka, H. and Hori, K. (1981). "Acoustoelastic Effect of Rayleigh Surface Wave in Isotropic Material." *Journal of Applied Mechanichs,* 48, 119-124.

Hughes, D. S. and Kelly, J. L. (1953). "Second-Order Elastic Deformation of Solids." *Physical Review*, 92(5), 1145-1149. December 1953.

Hurlebaus, S. (2002). "Laser Ultrasonics for Structural Health Monitoring." *Contribution to the 7th Laser-Vibrometer Seminar, Polytec, Waldbronn*, 1, 1-27.

Hurlebaus, S. (2005). "Smart Structures." Zachary Department of Civil Engineering, Texas A&M University.

Hurlebaus, S. and Jacobs, L.J. (2006). "Dual Probe Laser Interferometer for Structural Health Monitoring." *Journal of the Acoustical Society of America,* 119(4), 1923-1925.

Husson, D., Bennet, S.D., Kino, G.S. (1982). "Measurement of Surface Stresses Using Rayleigh Waves." *Ultrasonic Symposium*, 889-892.

Junge, M. (2003). "Measurement of Applied Stresses Using the Polarization of Rayleigh Surface Waves." M.S. Thesis, University of Stuttgart, Stuttgart, Germany.

Kil, H. G., Jarzynski, J., and Berthelot, Y. H. (1998). "Wave Decomposition of the Vibrations of a Cylindrical Shell with an Automated Scanning Laser Vibrometer." *Journal of the Acoustical Society of America*, 104(6), 3161-3168.

Kish, A. and Read, D. (2006): "11th Annual AAR Research Review." *Transportation Technology Center Inc. (TTCI)*, Pueblo, CO.

Kish, A., and Samavedam, G. (2005). "Improved Destressing of Continuous Welded Rail for Better Management of Rail Neutral Temperature." *Journal of the Transportation Research Board,* 1916, 56-65.

Masserey, B., and Fromme, P. (2008). "On The Reflection of Coupled Rayleigh-like Waves At Surface Defects in Plates." *Journal of the Acoustical Society of America,* 123, 88 - 98.

Murnaghan, F. D. (1951). *Finite Deformation of an Elastic Solid*. Wiley, New York.

MAPS Technology (2007). "15th Annual AAR Research Review." *Transportation Technology Center Inc. (TTCI)*, Pueblo, CO.

Net Resources International. "VERSE equipment." http://www.railway-technology.com /contractors/track/vortok/. October 2010.

Pao, Y. H. and Gamer, U. (1985). "Acoustoelastic Waves in Orthotropic Media." *Journal of the Acoustical Society of America*, 77(3), 806.

Pao, Y. H., and Sachse, W., and Fukuoka, H. (1984). "Acoustoelasticity and Ultrasonic Measurements of Residual Stresses." *Physical Acoustics,* 17, 61-143.

Rose, L. (1999). *Ultrasonic Waves in Solid Media*. Cambridge University Press, Cambridge, UK.

Smith, R.T., Stern, R., and Stephens, R.W.B. (1966). "Third-Order Elastic Moduli of Polycrystalline Metals from Ultrasonic Velocity Measurements." *Journal of the Acoustical Society of America*, 40(5), 1002-1008.

Telegraph Media Group. "Rail buckling". http://www.telegraph.co.uk/news/picturegaller ies/worldnews/4360255/Heatwave-in-Melbourne-plays-havoc-with-the-Australian-Open.html. October 2010.

Toupin, R.A., and Bernstein, B. (1961). "Sound Waves in Deformed Perfectly Elastic Materials." *Journal of the Acoustical Society of America*, 33(2), 216-225.

Tunna, J. (2000). "Vertical Rail Stiffness Equipment (VERSE) TRIALS." *Letter Report* for Vortex International, Transportation Technology Center Inc. (TTCI), Pueblo, CO.

Viktorov, I.A. (1966). *Rayleigh and Lamb Waves*. Plenum Press, New York.

VITA

Name	Ferdinand Djayaputra
Address	Zachry Department of Civil Engineering
	c/o Dr. Stefan Hurlebaus
	Texas A&M University
	College Station, Texas 77840
	Email: d_n4nd@tamu.edu
Education	B.S., (Civil Engineering) Texas A&M University, College Station, 2008.
	M.S., (Civil Engineering) Texas A&M University, College Station, 2010.